Study of Acetone Photodissociation over the Wavelength Range 248−330 nm: Evidence of a Mechanism Involving Both the Singlet and Triplet Excited States†

Mark A. Blitz,* Dwayne E. Heard, and Michael J. Pilling

School of Chemistry, University of Leeds, Leeds, U.K. LS2 9JT

Received: October 31, 2005; In Final Form: January 5, 2006

Measurements of the acetyl yield from acetone photolysis have been made using laser flash photolysis/laser induced fluorescence. $\Phi_{total}(\lambda,p,T)$ was determined over the ranges: $266 \leq \lambda/\text{nm} \leq 327.5$, $0.3 \leq p/\text{Torr} \leq 400$ and $218 \leq T/\text{K} \leq 295$. The acetyl yield was determined relative to that at 248 nm by conversion to OH by reaction with O_2. Linear Stern−Volmer plots (1/[OH] vs [M]) describe the data for $\lambda < 300$ nm, but for $\lambda > 300$ nm, nonlinear Stern−Volmer plots were observed. This behavior is interpreted as evidence for dissociation from two excited states of acetone: S_1 when the Stern−Volmer plots are linear and both S_1 and T_1 when Stern−Volmer plots are nonlinear. A model for acetone photolysis is proposed that can adequately describe both the present and literature data. Barriers to dissociation are invoked in order to explain the dependence of pressure quenching of the acetone photolysis yields as a function of wavelength and temperature. This pressure quenching was observed to become more efficient with increasing wavelength, but it was only above ~300 nm that a significant T dependence was observed, which became more pronounced at longer wavelengths. This is the first study to observe a T-dependent $\Phi_{total}(\lambda,p,T)$. A parametrized expression for $\Phi_{total}(\lambda,p,T)$ has been developed and is compared against the recommended literature data by running box model simulations of the atmosphere. These simulations show that acetone photolysis occurs more slowly at the top of the troposphere.

1. Introduction

The photoexcitation of acetone from the ground electronic state (S_0) to its first electronically excited state (S_1) has been intensively studied over many decades. This electronic transition in acetone results in a weak and broad absorption band from 220 to 330 nm with its maximum around 280 nm[1] and involves a perpendicular transition from the *n* orbital of the oxygen atom to the π^* orbital of the carbonyl group. From S_1, several intramolecular photophysical processes have been identified: [2−4] fluorescence via the $S_1 \rightarrow S_0$ transition, intersystem crossing (ISC) to the triplet state (T_1), and internal conversion to the hot ground state (S_0^*). The zero-pressure fluorescence quantum yield is only ~0.002,[5] but this is sufficient for acetone to be employed as a tracer in laser induced fluorescence (LIF) measurements of concentration and temperature in combustion engines.[6,7] This low fluorescence quantum yield implies that the nonradiative processes dominate.

Photoexcitation of acetone is known to result in cleavage of one of the α-CC bonds (Norrish type I)

$$(CH_3)_2CO + h\nu \rightarrow CH_3CO + CH_3 \qquad \text{(R1a)}$$

On the basis of the state-correlation diagram the α-cleavage of $S_1(n,\pi^*)$ to produce a bent acetyl fragment is symmetry forbidden. However, dissociation to produce acetyl in a linear configuration is symmetry allowed.[8] This geometry change in acetyl results in a barrier which, based on the most recent ab initio calculations, lies 556 kJ mol^{-1} (216 nm) above the zero point energy of S_0.[9] This barrier has been invoked in the literature to propose that acetone photodissociation does not occur via S_1. ISC to T_1 is known to be efficient,[4] and α-cleavage in excited acetone is postulated to occur from T_1. The accepted overall mechanism for acetone photodissociation can be described by Scheme 1.

The dissociation wavelength threshold from T_1 has been reported to be 305.8 nm,[10] based on the sudden loss of emission from acetone. This represents a barrier of 56 kJ mol^{-1} on the T_1 surface, assuming the T_1 state's origin is at 335 kJ mol^{-1}.[4]

The magnitude of the rate coefficients k_{ISC} and k_{dT} of Scheme 1 have been determined, but there are inconsistencies in the literature concerning their magnitudes. Over the wavelength range of 260−313 nm, Breuer and Lee[11] measured a nanosecond emission lifetime for excited acetone, which was equated to $1/k_{ISC}$. This nanosecond lifetime is consistent with the isotropic methyl product distribution observed by North et al.;[12] a long-lived excited state ensures that any initial alignment is lost. However, recent femtosecond mass spectrometry experiments have observed the rapid loss, <200 fs, of excited-state acetone together with the formation of acetyl. Shibata and Suzuki[13] argued that the persistent acetyl signal provides evidence for a long-lived excited state of acetone; the short-lived acetone excited state was assigned to a probe induced ionization effect. On the other hand, Castleman et al.[14,15] and Baronavski et al.[16] using essentially the same dataset concluded that dissociation from excited-state acetone is a femtosecond process. This rapid dissociation in excited-state acetone is consistent with a Rice−Ramsperger−Kassel−Marcus (RRKM) calculation on the triplet surface, T_1.[17]

Another feature of acetone dissociation is the occurrence of a three fragment photodissociation at shorter wavelengths

$$(CH_3)_2CO + h\nu \rightarrow CH_3 + CH_3 + CO \qquad \text{(R1b)}$$

† Part of the special issue "David M. Golden Festschrift".

* To whom correspondence should be addressed. E-mail: m.blitz@chem.leeds.ac.uk.

10.1021/jp056276g CCC: $33.50
Published on Web 02/04/2006

SCHEME 1

$$(CH_3)_2CO(S_0) \xrightarrow{h\nu} (CH_3)_2CO(S_1)$$

$$\downarrow k_{ISC}$$

$$(CH_3)_2CO(T_1) \xrightarrow{k_dT} CH_3CO + CH_3$$

North et al.[12] measured the translational energy of the methyl radical and showed that the overall three-body dissociation occurs via a stepwise mechanism, that is, the second methyl is formed from a vibrationally excited acetyl. At 248 nm, their data showed that 30% of the acetyl radicals undergo secondary dissociation. In a separate study, they determined the barrier for acetyl dissociation to be 71 kJ mol^{-1}.[18] Combining the acetyl barrier height with the thermodynamic limit for channel 1b, 299 nm, implies that the threshold for channel 1b is 254 nm. This is consistent with Waits et al.[19] who found no evidence for CO production when photolyzing acetone at 266 nm.

In this paper, we investigate various features of the acetone photodissociation mechanism. The acetyl radical was monitored using LIF by following the OH formed from the reaction between $CH_3CO + O_2$. When the yield of acetyl from acetone photolysis at various wavelengths is compared, the onset of the three fragment photodissociation, R1b, was observed. The lifetime of excited-state acetone was probed by varying the total pressure. Dissociation from excited-state acetone, $(CH_3)_2CO^*$, competes with collisional deactivation

$$(CH_3)_2CO(S_0) \xrightarrow{h\nu} (CH_3)_2CO^* \xrightarrow{k_d} CH_3 + CH_3CO \qquad \text{(R1a)}$$

$$(CH_3)_2CO^* + M \xrightarrow{k_M} (CH_3)_2CO(S_0) \qquad \text{(R1q)}$$

where k_d is the dissociation rate coefficient and k_M is the pressure quenching rate coefficient. The data show that dissociation occurs on a nanosecond or longer time scale from both S_1 and T_1 states.

Significant concentrations of acetone have been observed in the upper troposphere[20] where photolysis via R1a forms CH_3CO_3 and CH_3O_2 which are both potential sources of HO_x ($HO_x = OH + HO_2$).[21] To predict the radical yields from acetone photolysis, an accurate account of the pressure, temperature, and wavelength dependences of the quantum yield is required. In this present study, we thoroughly investigate the pressure quenching of acetone over a range of wavelengths relevant to atmospheric chemistry and show that, under atmospheric conditions, the photolysis yield at the longer wavelengths is much smaller than that given in the literature.[22,23] In addition, the photolysis yield at the longer wavelengths shows a strong temperature dependence which previous studies have failed to observe.

Following a brief description, in section 2, of the experimental methodology, section 3 outlines the use of LIF from OH, generated from $CH_3CO + O_2$, as a marker for acetyl. Section 4 presents the temperature, pressure, and wavelength dependence of the acetyl yield, in the form of Stern−Volmer (SV) plots, which provide evidence for a mechanism involving dissociation from both the first excited singlet and triplet states. This mechanism is developed in section 5 allowing the data to be analyzed in section 6 to generate excited-state rate constants and quantum yields. In section 7, the acetone fluorescence and phosphorescence literature is reinterpreted in terms of the mechanism proposed in section 5. In section 8, parametrized expressions for the quantum yields are developed and used in a box model to investigate briefly the atmospheric implications of the results.

2. Experimental Section

The present apparatus is a slight modification on the slow flow, laser flash photolysis/LIF technique, which has been previously described.[24] The photolysis of acetone was provided by either the 248 nm output from an excimer laser (Lambda Physik, Minex) or the doubled output from a Nd:YAG (Spectron, SL803) pumped dye laser (Spectron, SL4000), using the appropriate dye to cover the range of 279−327.5 nm. The laser wavelength was calibrated (±0.001 nm) using a wavemeter (Coherent, Wavemaster); 266 nm was generated by doubling the 532 nm output from the Nd:YAG laser. The excimer and dye laser outputs were counter-propagated through the reaction cell, and the beams were shaped using irises in order that they essentially defined the same volume in the reaction zone—the volume defined by the photolysis/probe laser beam overlap. The output energy from the dye laser was typically a few millijoules, and the excimer laser energy was adjusted using a combination of neutral density filters to give a comparable amount of photolysis. The energy of the lasers was determined by averaging the output of an energy meter (Gentec ED-200LA) over typically 50 laser pulses. The OH produced in the reaction cell was probed using off-resonant LIF via the $A^2\Sigma^+$, ($\nu = 1$) ← $X^2\Pi_i$, ($\nu = 0$) $Q_1(1)$ transition at ∼282 nm using the doubled output from an Nd:YAG (Spectra Physics, Quanta-Ray GCR150) pumped dye laser (Spectra Physics, Quanta Ray PDL-3, Rhodamine 6G). This probe light was defocused and entered the reaction cell at right angles to the photolysis lasers and at the reaction zone was ≥1.5 cm in diameter. Perpendicular to the reaction zone two internally mounted planar convex lenses ($f = 4.0$ cm) were used to image the OH fluorescence; the lenses were arranged to image the reaction zone at the window of the cell. Beyond the window, the fluorescence passed through an iris, which was adjusted to match the diameter of the probe laser and an interference filter before being detected using a photomultiplier (EMI 9813). The photomultiplier signal was integrated with a boxcar averager (SR250), which was adjusted to exclude the first 50 ns following the probe laser and digitized before being passed to a personal computer for subsequent data analysis. The computer was interfaced to a delay generator (SRS 535) to control the delay time between the photolysis laser and probe laser. Temporal profiles of OH consisted of 100 time points, with each point averaged over 4−8 laser shots. The pulse repetition frequency of the lasers was 5 Hz.

Mass flow meters (MKS) were used to control the flow of the acetone, O_2, and the buffer gas. Helium was the main buffer gas, but there were a number of experiments where N_2, O_2, and air were also used. Pressures in the cell were measured using capacitance manometers (MKS) and were adjusted by throttling the exit valves on the cell; the pressures were adjusted between 0.3 and 400 Torr. The total flow ensured that there was no significant degradation of the sample between laser shots. An insulated metal box around the six-way-cross reaction cell containing stirred, refrigerated methanol allowed temperature control, enabling experiments to be performed over the range of 218−295 K. Acetone (Aldrich, HPLC grade) was degassed and diluted in He. Helium (BOC, CP grade, 99.999%), N_2 (Air Products, 99.999%), O_2 (Air Products, high purity, 99.999%), and air (Air Products) were used straight from the cylinder.

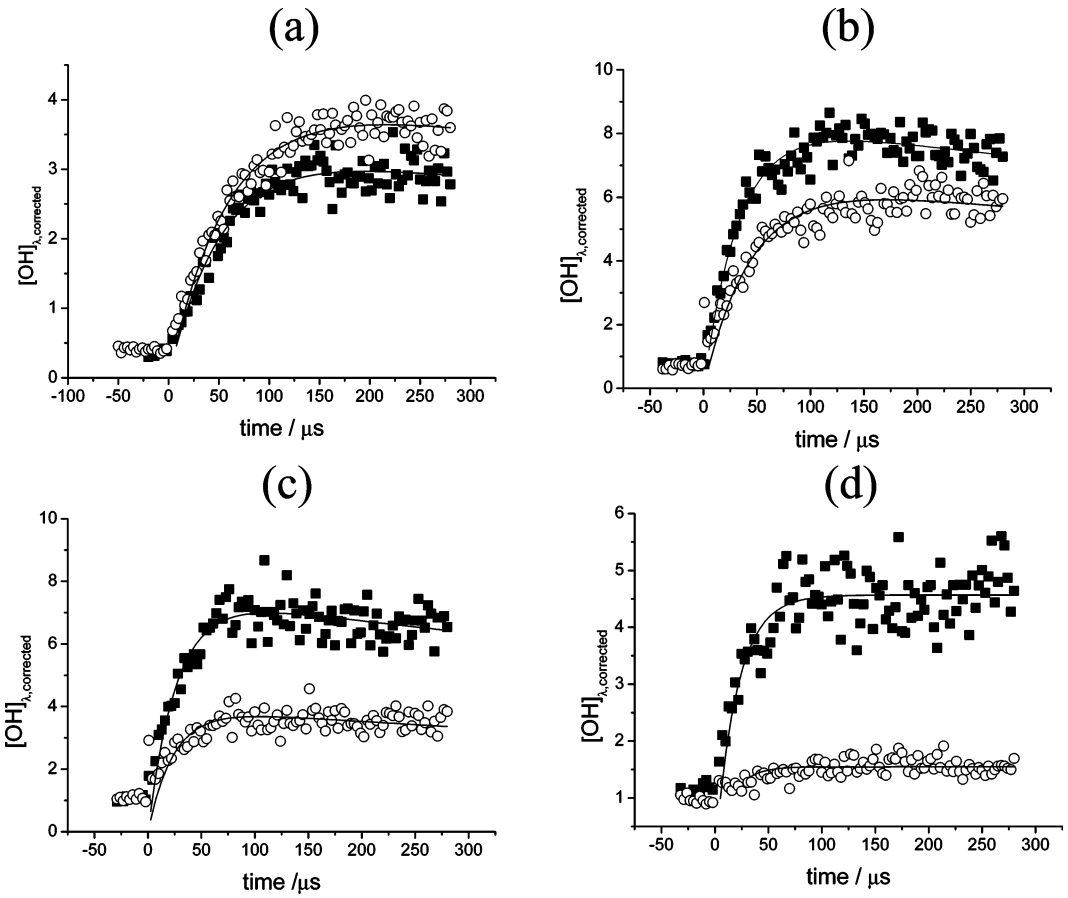

Figure 1. Biexponential time profiles for the $OH_{\lambda,corrected}$ LIF signal following pulsed photolysis of acetone in the presence of O_2 and various total pressures of He at 295 K: filled squares = 248 nm and open circles = 308 nm. Solid lines represent fits to the data. $\alpha[CH_3CO]_0$ is approximately equal to the maximum OH signal from the kinetic trace. In plot (a), [M] = 6 Torr and $\alpha[CH_3CO]_{0,308}$ is greater than $\alpha[CH_3CO]_{0,248}$; this reflects the substantial three-body dissociation (R1b) occurring at 248 nm. However, as the total pressure is increased, (b) = 50 Torr, (c) = 100 Torr, and (d) = 400 Torr, $\alpha[CH_3CO]_{0,308}$ falls increasingly below $\alpha[CH_3CO]_{0,248}$; this demonstrates pressure quenching in the excited state of acetone.

3. Methodology: Use of OH Laser Induced Fluorescence from $CH_3CO + O_2$

In a recent letter, we reported the formation of OH from $CH_3CO + O_2$ by a chemical activation route where OH formation competes with collisional stabilization to form the peroxyacetyl radical[24]

$$CH_3CO + O_2 + M \rightarrow CH_3CO(O)_2 + M \qquad \text{(R2a)}$$

$$CH_3CO + O_2 \rightarrow OH + \text{other products} \qquad \text{(R2b)}$$

OH can be detected with great sensitivity using LIF; [OH] $\leq 10^8$ molecule cm^{-3} is readily detected in this study. Reaction 2 therefore provides a method for directly determining the CH_3CO yield from acetone photolysis, given sufficient O_2 to convert the acetyl to OH. To date, there have been no direct determinations of the radical yield of from acetone photolysis as a function of pressure, because both the acetyl and methyl radicals are difficult to detect with good sensitivity at pressures up to 1 atm. It should be noted that while reaction 2 provides a convenient means of detection for CH_3CO, as the total bath gas concentration, [M], increases, reaction R2a starts to dominate over reaction R2b and the sensitivity of the technique is reduced. Even at 400 Torr total pressure, however, reaction R2b still contributes ~10% to the overall reaction.[24] Other studies of the quantum yield have relied upon end product analysis. However, the present direct technique has the advantage of much greater sensitivity and hence allows a much more rapid accumulation of quantum yield determinations; this advantage is significant given the complex dependence of the quantum yield on wavelength, temperature, and pressure.

Figure 1 shows a biexponential time profile for the OH LIF signal following pulsed photolysis of acetone in the presence of O_2 and He. [OH] is given by the equation

$$[OH] = \frac{\alpha[CH_3CO]_0 k_2'}{k_2' - k_3}[\exp(-k_3 t) - \exp(-k_2' t)] \qquad \text{(E1)}$$

where $k_2' = k_2[O_2]$ and k_2 is the overall, pressure-dependent second-order rate constant for reaction 2, k_3 is the first-order rate constant for the loss of OH by reaction with acetone and by diffusion, α is the fractional yield of OH in reaction R2, that is, $\alpha = k_{2b}/(k_{2a} + k_{2b})$, and $[CH_3CO]_0$ is the initial acetyl concentration from pulsed photolysis.

The experimental data were fitted to eq E1 to yield $\alpha[CH_3CO]_0$. Because the OH determination is based on laser induced fluorescence measurement, this value of $\alpha[CH_3CO]_0$ is only relative. Since α is pressure dependent, it is essential that comparisons of $\alpha[CH_3CO]_0$ at various photolysis wavelengths are made at the same total pressure if relative quantum yields of the acetyl radical are to be obtained. There remains the question of any wavelength dependence of the OH yield that could arise if the acetyl radical reacted with O_2 before it was fully thermalized. Under experimental conditions, the CH_3CO radicals undergo more than 1000 collisions before reaction with oxygen. They are therefore expected to be fully thermalized,

and the OH yield is expected to be independent of photolysis wavelength. Also, nonthermalized radicals might be expected to be revealed from their pressure dependence, but no such behavior was observed, which is especially evident in the short wavelength data where little or no pressure dependence was observed.

The acetone photolysis measurements were made relative to the acetyl radical yield at 248 nm. At this wavelength, the excited state of acetone is sufficiently short-lived such that pressure quenching is inefficient, as shown by the measurements of Gierczak et al.,[22] who found the quantum yield independent of pressure up to 760 Torr and Aloisio et al.[25] who obtained similar results at pressures up to 100 Torr. Note, however, that the acetyl radical is formed with sufficient internal energy that some further fragmentation occurs (reaction R1b); although the quantum yield for acetyl formation at 248 nm is less than unity, it remains pressure independent at 248 nm. The lack of a pressure dependence in the yield at 248 nm allows it to be used as a reference to enable the reduction in quantum yield with pressure to be determined at the longer wavelength. We also discuss below methods for placing the CH_3CO quantum yields on an absolute basis.

4. Stern−Volmer Plots for the Acetyl Yield

Figure 1 shows paired traces of OH formation at 248 and 308 nm over a range of pressures. These data are well described by eq E1 and yield relative values of $\alpha[CH_3CO]_0$. Note that because the loss of OH is very slow, the apparent OH limit is approximately equal to $\alpha[CH_3CO]_0$. In general, each pair of traces returned a similar value of k_3, which had little effect on $\alpha[CH_3CO]_0$. Occasionally, mainly at low pressures where OH loss due to diffusion could be significant, each pair of traces was analyzed using a fixed k_3 value. This fixed value for k_3 was determined from one of the pairs of traces or from separate longer time experiments; each pair of traces should have equal OH removal kinetics. Overall, as long as k_3 is either small compared to k_2' or directly determined, then a consistent determination of $\alpha[CH_3CO]_0$ can be made via E1.

The traces demonstrate clearly the effects of collisional quenching of the excited state at the higher pressures. At 6 Torr, more CH_3CO was formed at $\lambda = 308$ nm compared to the reference wavelength, 248 nm, but as the pressure was increased, the CH_3CO yield at the longer wavelength progressively decreased below that at the reference wavelength. This reduction in $\alpha[CH_3CO]_0$ at the wavelength of interest, relative to that at 248 nm, is due to collisional quenching of the excited state of acetone via R1q.

The data, as shown in Figure 1, were corrected for differences in laser photon intensity, I (energy/$h\nu$), and acetone absorption cross-section. The laser energies were determined by averaging the output of the energy meter over typically 50 laser pulses, and the absorption cross-sections were taken from Gierczak et al.[22] The raw OH signal, $[OH]_{\lambda,\text{uncorrected}}$, at the wavelength of interest was normalized relative to that at 248 nm using the expression

$$[OH]_{\lambda,\text{corrected}} = \frac{I_{248\text{nm}}}{I_\lambda} \times \frac{\sigma_{248\text{nm}}}{\sigma_\lambda} \times [OH]_\lambda,\text{uncorrected} \quad \text{(E2)}$$

The laser energy at 248 nm was adjusted, using neutral density filters, to give OH signals of similar magnitudes at the two wavelengths at the lowest pressure, minimizing the errors that propagate when corrected using eq E2. The values of $[OH]_{\lambda,\text{corrected}}$ and $[OH]_{248\text{nm}}$ were analyzed using eq E1 to yield

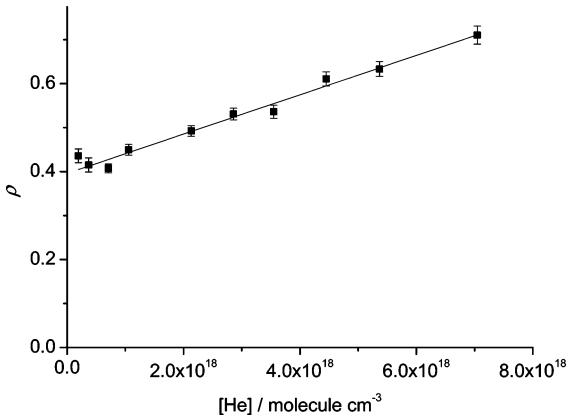

Figure 2. Example of a linear SV plot for acetone photolysis at 299 nm and 273 K with He buffer gas. The parameters of this plot are given in Table 1.

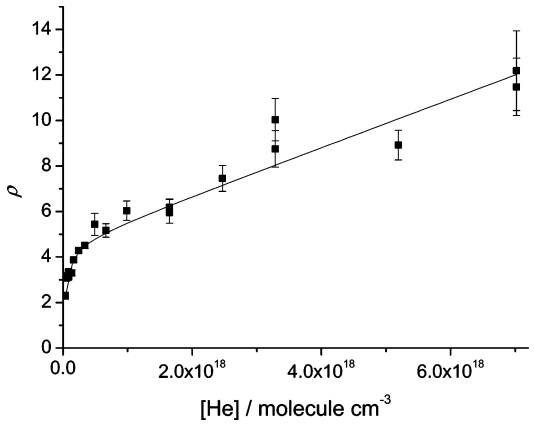

Figure 3. Example of a nonlinear SV plot for acetone photolysis at 320 nm and 295 K with He buffer gas. The parameters of this plot are given in Table 2.

$\alpha[CH_3CO]_{0,\lambda\ \text{corrected}}$ and $\alpha[CH_3CO]_{0,248\text{nm}}$, respectively. The ratio of the two, $\rho = \alpha[CH_3CO]_{0,248\text{nm}}/\alpha[CH_3CO]_{0,\lambda\text{corrected}} = [CH_3CO]_{0,248}/[CH_3CO]_{0,\lambda}$ (the nm and corrected subscripts are now omitted) provided α is independent of wavelength.

The collisional quenching of fluorescence is generally described by the SV relationship

$$\rho = [CH_3CO]_{0,248}/([CH_3CO]_{0,\lambda} = 1 + A[M] \quad \text{(E3)}$$

where A is the SV quenching parameter and is equal to τk_M where τ is the lifetime of the excited state, k_M is the collision quenching rate constant, and [M] is the concentration of the buffer gas. Equation E3 only applies if the yield of acetyl at 248 nm is pressure independent. From this equation, a plot of ρ vs [M] yields a straight line with slope equal to A. Figure 2 shows a SV plot for 299 nm which exhibits good linearity and an intercept of ~0.40. Figure 3 shows a plot at 320 nm which shows quite different nonlinear behavior. These two types of behavior corresponded to different wavelength ranges, with linear SV plots below ~300 nm and nonlinear plots above ~300 nm. The degree of nonlinearity increased as the wavelength increased, as did the total amount of quenching in the system.

This behavior is compatible with quenching of (at least) two excited states with different lifetimes. At wavelengths above ~300 nm, the low-pressure, high-slope section of the SV plot involves quenching of a longer-lived state, and the lower-slope section at higher pressures involves a shorter-lived excited state. It seems reasonable to identify these two states as the first excited singlet (S_1, shorter-lived) and triplet (T_1, longer-lived)

states of acetone. The next section develops a model based on this assignment.

The values of $[CH_3CO]_{0,248}/[CH_3CO]_{0,\lambda}$ were determined over the wavelength range $\lambda = 266-330$ nm. Each determination of $[CH_3CO]_{0,248}/[CH_3CO]_{0,\lambda}$ was derived from a pair of kinetic traces, see Figure 1, which were always recorded within a period of 5 min. For any given SV plot, up to 20 $[CH_3CO]_{0,248}/[CH_3CO]_{0,\lambda}$ determinations were made with the pressure varied randomly. This method of randomly varying the pressure combined with rapid data accumulation helped avoid the effects of systematic errors such as wavelength drift in the OH probe laser. The concentration of acetone used was typically 100 mTorr but was varied by up to a factor of 3 depending on the wavelength; the criterion was to maintain a good OH signal. When either He or N_2 was used as the buffer gas, the O_2 concentration was typically 300 mTorr, and when either air or O_2 were used, the concentration of O_2 was determined from the total pressure. The dye laser photolysis energy was typically 5 mJ/pulse. Consequently, at longer wavelengths, where the acetone absorption cross-section is much smaller, the energy of the 248 nm reference laser was accordingly reduced in order to approximately match the two OH signals at low pressure.

5. Model for the Dissociation of Acetone via the S_1 and T_1 States

Two wavelength regions will be considered, below and above 300 nm. ISC is only incorporated in the model for the longer wavelength range.

The proposed mechanisms for $\lambda < 300$ nm is

$$S_0 + h\nu \rightarrow S_1, S_1^*$$

$$S_1 \rightarrow CH_3CO + CH_3 \quad k_{dSa}$$

$$S_1^* \rightarrow 2CH_3 + CO \quad k_{dSb}$$

$$S_1 + M \rightarrow S_0 + M \quad k_{MS}$$

where S_0, (S_1, S_1*), and T_1 are the ground, first excited singlet states, and the first excited triplet state, respectively. The quantum yield for fluorescence from excited acetone is small [5] and consequently is not included in the mechanism. S_1* is the fraction of S_1 which has sufficient energy (see section 6c) to dissociate to CO. The literature suggests [26−28] that the CO yield is independent of total pressure at all wavelengths, and hence, the quenching of S_1* by the buffer gas is not included in the above scheme. If there is quenching of S_1* that competes with dissociation, then our reported acetone photolysis yields would overestimate the true values, but as the yield of CO at wavelengths ≥280 nm is increasingly less than 0.15, see section 6c, the omission of S_1* quenching should not significantly affect our results.

The above scheme implies that the acetyl radical and CO are formed through independent channels.

The ratio of the CH_3CO yields, integrated over the photolysis pulses, at 248 nm and at λ is given by

$$\rho = \frac{[CH_3CO]_{0,248}}{[CH_3CO]_{0,\lambda}} = \frac{\beta_{248}}{\beta_\lambda}\left(1 + \frac{k_{MS}}{k_{dSa}}[M]\right)_\lambda = \frac{\beta_{248}(1 + a_1[M])_\lambda}{\beta_\lambda} \quad \text{(E4)}$$

where $a_1 = k_{MS}/k_{dSa}$ and $\beta = k_{dSa}/k_{dS}$ ($k_{dS} = k_{dSa} + k_{dSb}$) and is equal to the CH_3CO yield at zero pressure. Equation E4 is of the form expected for a linear SV plot, with a slope/intercept ratio equal to a_1.

For $\lambda > 300$ nm, the mechanism includes ISC and dissociation from and quenching of T_1

$$S_0 + h\nu \rightarrow S_1, S_1^*$$

$$S_1 \rightarrow CH_3CO + CH_3 \quad k_{dSa}$$

$$S_1^* \rightarrow 2CH_3 + CO \quad k_{dSb}$$

$$S_1 \rightarrow T_1 \quad k_{ISC}$$

$$S_1 + M \rightarrow S_0 + M \quad k_{MS}$$

$$T_1 \rightarrow CH_3CO + CH_3 \quad k_{dT}$$

$$T_1 + M \rightarrow S_0 + M \quad k_{MT}$$

For reasons which will be discussed more fully below, the triplet state dissociation results only in the formation of $CH_3CO + CH_3$. The ratio of the acetyl yields now takes the following form

$$\rho = \frac{[CH_3CO]_{0,248}}{[CH_3CO]_{0,\lambda}} = \frac{\beta_{248}}{\beta_\lambda}\frac{(1 + a_2 + a_1[M])(1 + a_3[M])}{(1 + a_2 + a_3[M])} \quad \text{(E5)}$$

where $a_2 = k_{ISC}/k_{dSa}$ and $a_3 = k_{MT}/k_{dT}$. Clearly, a SV plot of ρ vs [M] will be nonlinear. The data analysis reported below for $\lambda > 300$ nm employed the full form of eq E5 in a nonlinear least-squares fit. It is instructive, however, to examine the intercept, c_1, of eq E5 at [M] = 0 and the extrapolated intercept, c_2, and slope, m, for the high-pressure linear section of the plot (Figure 3)

$$c_1 = \frac{\beta_{248}}{\beta_\lambda} \quad \text{(E6)}$$

$$c_2 = \frac{\beta_{248}(1 + a_2)_\lambda}{\beta_\lambda} \quad \text{(E7)}$$

The ratio of these two intercepts is

$$\frac{c_2}{c_1} = 1 + a_2 = 1 + \frac{k_{ISC}}{k_{dSa}} \quad \text{(E8)}$$

$$m = a_1\frac{\beta_{248}}{\beta_\lambda} = \frac{\beta_{248}}{\beta_\lambda}\left(\frac{k_{MS}}{k_{dSa}}\right)_\lambda \quad \text{(E9)}$$

The equation for m is identical to the slope of eq E4 as expected, since the high-pressure linear section relates to the quenching of S_1.

This proposed mechanism for acetone photolysis does not include fluorescence or phosphorescence from the excited states as they occur only to a minor extent.[5,29] This proposed mechanism is summarized in the schematic in Figure 4, which includes the energetics for the various processes, but three-body dissociation via S_1* to $2CH_3 + CO$ has been omitted on the grounds of clarity. Figure 4 should be referred to in the following sections as a quick guide to the mechanism of the system.

6. Testing the Model for Acetone Photolysis

(a) $\lambda < 300$ nm. The data for $\lambda \leq 300$ nm were fitted to the SV relationship, eq E4, using a weighting equal to the error in

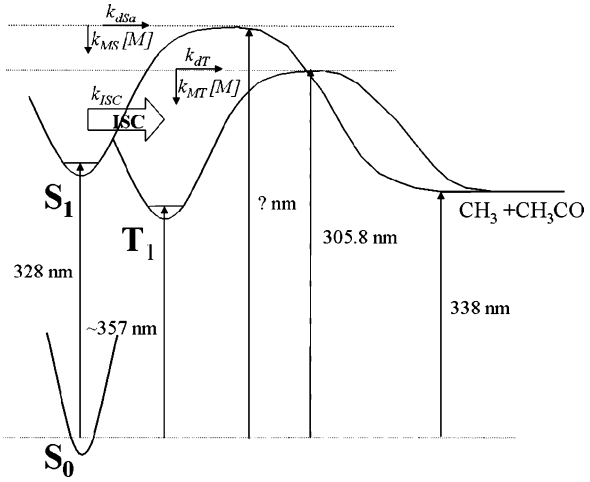

Figure 4. Schematic of the energetics and mechanism for acetone photolysis: $(CH_3)_2CO + h\nu \rightarrow (CH_3)_2CO(S_1)$ ($\lambda_{threshold} = 328.6$ nm),[33] $(CH_3)_2CO + h\nu \rightarrow (CH_3)_2CO(T_1)$ ($\lambda_{threshold} = 357$ nm),[4] $(CH_3)_2CO(T_1) \rightarrow CH_3CO + CH_3$ ($\lambda = 305.8$ nm relative to S_0),[10] $(CH_3)_2CO(S_1) \rightarrow CH_3CO + CH_3$ ($\lambda =$? nm, the unknown barrier height), and $(CH_3)_2CO + h\nu \rightarrow CH_3CO + CH_3$ ($\lambda = 338$ nm).[22] Also, see section 5 for a further description of the model for acetone dissociation.

$[CH_3CO]_{0,248}/[CH_3CO]_{0,\lambda}$. An example of such a plot is shown in Figure 2, which shows errors increasing at the highest pressures due to a reduced OH signal; errors for all the $\lambda <$ 300 nm data were <10%. The returned parameters are given in Table 1. From Table 1, it is observed that the intercepts are less than 1.0, implying that $[CH_3CO]_{0,248}$ is less than $[CH_3CO]_{0,\lambda}$. This is a consequence of a greater fraction of acetone photolysis occurring via three-body dissociation (R1b) at 248 nm compared to the wavelength under investigation, λ. In the model developed in section 5, this effect was taken into account by introducing k_{dSb} ($S_1^* \rightarrow 2CH_3 + CO$) and the results in eq E4, where the intercept of the SV relationship is equal to $\beta_{248}/\beta_\lambda$, the ratio of zero pressure CH_3CO yields at 248 nm and λ. By dividing the slope by the intercept, eq E4 yields the S_1 quenching parameter, k_{MS}/k_{dSa}, and these values are given in the final column of Table 1. Inspection of the k_{MS}/k_{dSa} data reveals the effect of wavelength and T on quenching; this behavior is mainly related to the decrease in k_{dSa} with decreasing T. However, further discussion of k_{MS}/k_{dSa} is delayed until we also consider the data at longer wavelengths where the behavior is more revealing of the mechanism.

(b) $\lambda >$ 300 nm. The data for $\lambda >$ 300 nm were fitted to eq E5, using a weighting equal to the statistical error in $[CH_3CO]_{0,248}/[CH_3CO]_{0,\lambda}$. An example of such a fitting is shown in Figure 3. Weighting was increasingly important at long wavelengths where errors increased significantly, up to 30%, at higher pressures, due to the severe amount of quenching in the system. The $\beta_{248}/\beta_\lambda$ parameter in eq E5 was fixed to values extrapolated from analysis of the $\lambda <$ 300 nm data; see section 6c. $\beta_{248}/\beta_\lambda$ is almost constant for a given temperature with β_λ close to 1.0 for $\lambda \geq$ 300 nm. Equation E5 gave an excellent fit to all the data, and the returned parameters k_{MS}/k_{dSa}, k_{ISC}/k_{dSa}, and k_{MT}/k_{dT} are given in Table 2.

From Table 2 and the SV plots, several general features are observed. As expected, the SV slopes for both S_1 (k_{MS}/k_{dSa}) and T_1 (k_{MT}/k_{dT}) increase with increasing wavelength. Also, k_{ISC}/k_{dSa}, obtained from the ratio of intercepts shows that ISC becomes increasingly competitive with dissociation as λ is increased above 300 nm. As a result, dissociation via T_1 becomes increasingly important. Since $k_{dT} \ll k_{dSa}$, a_3[M] becomes large compared with $(1 + a_2)$ at quite low pressures.

TABLE 1: Returned Parameters from Linear Fitting to the $[CH_3CO]_{0,248}/[CH_3CO]_{0,\lambda}$ vs [M] Data[a]

λ/nm	T/K	buffer	intercept	10^4 slope/Torr^{-1}	10^{20} k_{MS}/k_{dSa}[b]
299	295	He	0.35 ± 0.02	8.63 ± 1.68	6.80
299	273	He	0.40 ± 0.01	15.8 ± 1.7	10.9
299	248	He	0.48 ± 0.02	22.4 ± 3.2	12.9
299	218	He	0.48 ± 0.01	45.1 ± 2.6	20.2
297	295	He	0.37 ± 0.01	18.2 ± 0.7	14.2
297	295	N_2	0.38 ± 0.01	23.0 ± 2.2	18.0
297	295	air	0.36 ± 0.01	23.4 ± 1.7	18.3
296	295	He	0.37 ± 0.02	5.48 ± 1.70	4.29
296	273	He	0.39 ± 0.02	15.3 ± 1.6	10.5
296	248	He	0.49 ± 0.02	8.92 ± 1.62	5.12
296	218	He	0.51 ± 0.01	31.3 ± 2.0	14.0
295.5	295	He	0.37 ± 0.01	17.4 ± 0.9	13.6
292	295	He	0.41 ± 0.02	9.66 ± 2.46	7.49
292	273	He	0.46 ± 0.02	11.3 ± 2.1	7.77
292	248	He	0.48 ± 0.02	19.1 ± 2.2	11.0
292	218	He	0.47 ± 0.02	17.4 ± 2.4	7.77
292	295	N_2	0.36 ± 0.01	10.7 ± 1.8	8.30
292	295	air	0.38 ± 0.01	14.9 ± 2.7	11.6
291	295	He	0.38 ± 0.01	11.0 ± 0.6	8.50
288	295	He	0.37 ± 0.02	7.96 ± 1.54	6.08
288	273	He	0.43 ± 0.02	6.89 ± 1.86	4.72
288	248	He	0.43 ± 0.02	12.3 ± 2.6	7.06
288	218	He	0.49 ± 0.02	6.34 ± 1.84	2.83
288	295	N_2	0.43 ± 0.02	5.80 ± 2.72	4.43
288	295	air	0.39 ± 0.01	3.22 ± 2.42	2.46
286	295	He	0.39 ± 0.01	6.85 ± 0.80	5.18
286	295	N_2	0.44 ± 0.01	12.7 ± 2.7	9.61
286	295	air	0.38 ± 0.01	5.44 ± 2.32	4.12
284	295	He	0.40 ± 0.01	9.53 ± 1.04	7.13
284	295	N_2	0.41 ± 0.01	9.87 ± 2.12	7.39
284	295	air	0.40 ± 0.01	14.0 ± 1.7	10.5
283	295	He	0.41 ± 0.02	3.95 ± 1.80	2.94
283	273	He	0.44 ± 0.02	6.74 ± 1.64	4.59
283	248	He	0.49 ± 0.02	4.34 ± 1.50	2.49
283	218	He	0.54 ± 0.02	9.40 ± 2.00	4.20
282	295	He	0.41 ± 0.01	8.36 ± 0.78	6.18
282	295	N_2	0.33 ± 0.01	4.79 ± 1.28	3.54
282	295	air	0.42 ± 0.01	13.1 ± 2.1	9.68
280	295	He	0.40 ± 0.01	8.95 ± 0.88	6.52
280	295	N_2	0.43 ± 0.02	9.20 ± 2.96	6.70
280	295	Air	0.43 ± 0.01	33.9 ± 2.5	24.7
279	273	He	0.47 ± 0.02	11.3 ± 2.2	7.61
279	218	He	0.55 ± 0.02	11.6 ± 2.0	5.18
279	295	air	0.41 ± 0.01	11.9 ± 1.7	8.59
266	295	air	0.43 ± 0.01	10.5 ± 2.0	6.26
266	218	He	0.43 ± 0.02	4.25 ± 4.00	1.90
266	248	He	0.43 ± 0.02	8.04 ± 3.60	4.48
266	295	He	0.56 ± 0.02	6.43 ± 0.88	3.83
266	295	N_2	0.48 ± 0.01	6.47 ± 2.34	3.86

[a] From eq E4, k_{MS}/k_{dSa} is obtained from dividing the slope by the intercept. The data were weighted, and errors represent 2σ. [b] Units are in cm^3 molecule^{-1}.

This results in a linear, higher-pressure region of the SV plot, where the bracketed terms in a_3[M] cancel. The intercept (c_2) and slope (m) of this region are given by eqs E7 and E9. An example of this behavior is shown in Figure 5, where between 282 and 315 nm the intercept increases from ca. 0.4 to 2. This apparent increase in the intercept with wavelength reflects the increase in k_{ISC}/k_{dSa} with wavelength—see Table 2—resulting in a bigger T_1 population, which is rapidly quenched. This effect, as exemplified in Figure 5, has been observed previously in the studies by Meyrahn et al. and Gierczak et al.[22,30] A consistent mechanism to explain this behavior has been hampered by previous assumptions that dissociation occurs exclusively on the triplet surface, T_1 (see the introduction). However, any plausible explanation of the present data requires dissociation from more than one state. Recently, Emrich et al.[28] noted that triplet acetone, T_1, is rapidly quenched by oxygen, so that under

TABLE 2: Stern−Volmer Parameters for Acetone Quenching above 300 nm[a]

λ/nm	T/K	buffer	$10^{19}\ k_{MS}/k_{dSa}$[b]	k_{ISC}/k_{dSa}[b]	$10^{18}\ k_{MT}/k_{dT}$[b]
302	295	He	1.84 ± 0.20	~0	
302	273	He	2.12 ± 0.18	~0	
302	248	He	2.73 ± 0.22	~0	
302	218	He	3.53 ± 0.32	~0	
305.5	295	He	2.35 ± 0.44	0.21 ± 0.24	5.06 ± 5.80
305.5	273	He	3.55 ± 2.24	0.34 ± 4.4	9.49 ± 74.0
305.5	248	He	3.78 ± 1.60	0.59 ± 1.33	2.66 ± 7.18
305.5	218	He	6.40 ± 1.30	0.46 ± 0.62	6.80 ± 15.52
305.5	295	N_2	1.88 ± 3.84	0.70 ± 0.81	11.7 ± 28.8
308	295	He	4.56 ± 0.90	1.11 ± 0.46	6.67 ± 4.68
308	273	He	7.64 ± 1.52	0.92 ± 0.54	17.6 ± 27.4
308	248	He	11.1 ± 1.2	1.45 ± 0.32	40.4 ± 27.4
308	218	He	18.4 ± 2.5	2.59 ± 0.72	32.9 ± 18.8
308	295	N_2	5.22 ± 2.90	1.11 ± 0.68	12.9 ± 12.8
308	295	air	8.09 ± 5.02	0.95 ± 0.60	28.2 ± 39.0
310.5	295	He	6.34 ± 0.94	1.69 ± 0.28	35.1 ± 17.4
310.5	273	He	10.5 ± 2.6	1.79 ± 0.56	75.7 ± 90.4
310.5	248	He	19.5 ± 3.2	2.84 ± 0.56	70.8 ± 37.2
310.5	218	He	38.4 ± 11.6	3.67 ± 1.62	367 ± 1560
310.5	295	N_2	7.81 ± 8.42	2.14 ± 1.36	15.7 ± 8.4
310.5	295	air	12.2 ± 7.4	1.41 ± 1.02	49 ± 104
312.5	295	He	11.0 ± 2.8	3.12 ± 0.52	108 ± 78
312.5	273	He	25.7 ± 6.2	3.52 ± 0.82	168 ± 98
312.5	248	He	30.4 ± 13.6	4.82 ± 1.98	128 ± 100
312.5	218	He	70.0 ± 11.2	9.73 ± 1.62	462 ± 258
312.5	295	N_2	21.3 ± 7.3	1.77 ± 0.34	199 ± 127
315	295	He	13.3 ± 2.9	4.73 ± 0.86	96.6 ± 37.2
315	273	He	28.9 ± 6.0	5.48 ± 0.82	237 ± 88
315	248	He	58.0 ± 12.4	9.73 ± 1.20	279 ± 46
315	218	He	183 ± 37	18.8 ± 4.5	314 ± 62
317.5	295	He	27.9 ± 5.9	6.60 ± 0.86	166 ± 54
317.5	273	He	77.3 ± 15.4	8.53 ± 1.96	368 ± 260
317.5	248	He	129 ± 32	24.8 ± 4.4	505 ± 129
317.5	218	He	744 ± 806	51.0 ± 37.6	1173 ± 790
317.5	295	N_2	23.7 ± 13.2	5.35 ± 1.16	152 ± 85
320	295	He	27.7 ± 6.7	11.2 ± 1.1	273 ± 73
322.5	295	He	62.2 ± 30.6	15.1 ± 3.1	303 ± 145
322.5	295	N_2	18.9 ± 12.0	15.2 ± 3.8	599 ± 161
325	295	He	82.8 ± 30.9	15.7 ± 2.2	830 ± 394
327.5	295	He	126 ± 63	20.4 ± 2.7	3813 ± 5114

[a] Returned parameters are from non-linear least squares fitting of eq E5 to the $[CH_3CO]_{0,248}/[CH_3CO]_{0,\lambda}$ vs [M] data. The data were weighted, and errors represent 2σ. [b] Units for k_{MS}/k_{dSa} and k_{MT}/k_{dT} are cm^3 $molecule^{-1}$, and k_{ISC}/k_{dSa} is unitless.

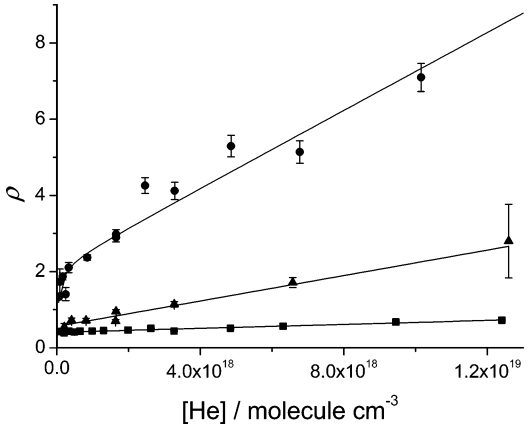

Figure 5. Example of the apparent increase in the intercept of the SV plot as the wavelength is increased: ■ = 282 nm, ▲ = 308 nm, and ● = 315 nm. All plots were made at 295 K with He buffer gas.

their conditions any observed reduction in dissociation yield with increasing pressure occurs exclusively from S_1.

For all our data, it was observed that the system was in this high-pressure regime, with linear SV plots, above 25 Torr, where only the first two parameters of Table 2 are required to describe the data; the previous data of Meyrahn et al., Gierczak et al., and Emrich et al.[22,27,28,30] were similarly determined at total pressures greater than 25 Torr. For modeling acetone photolysis in the atmosphere, this two-parameter high-pressure regime should be an adequate description under almost all conditions in the troposphere. However, in our experiments, we have performed additional experiments and reduced the oxygen concentration and the total pressure such that the triplet state, T_1, is not completely quenched. The resulting nonlinear SV behavior is shown in Figure 3 for 320 nm. At low pressure, the steep slope of the SV plot is due to the quenching of the triplet state, and at high pressure, the SV plot describes the quenching of the singlet state. Figure 3 alone shows the low- and high-pressure features of eq E5 and hence provides support for the proposed acetone photolysis mechanism. In the next section, we examine individually the three parameters in Table 2 to further validate the proposed mechanism and to explore the features of the excited-state surfaces and their coupling. Figure 4 shows a proposed potential energy diagram.

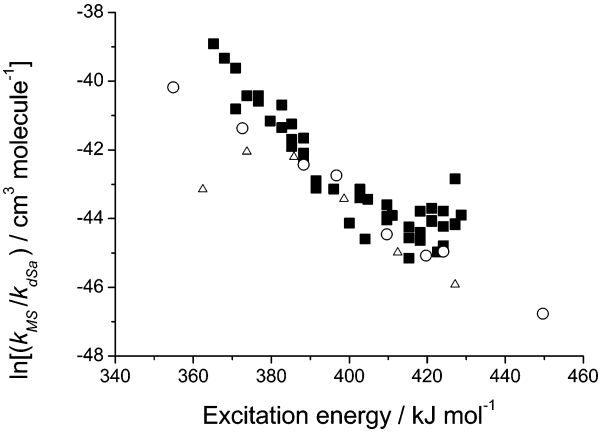

Figure 6. Plot of $\ln(k_{MS}/k_{dSa})$ vs excitation energy (photolysis wavelength) for our data together with the literature data: ■ = Leeds, △ = Warneck et al.,[23] and ○ = Gierczak et al.[22]

***k_{MS}/k_{dSa}* Parameter.** Table 2 shows that quenching from the singlet state, k_{MS}/k_{dSa}, increases strongly with wavelength. This dependence is almost exclusively associated with a decrease in k_{dSa} with increasing λ. The quenching rate constant, k_{MS}, is expected to vary only a little with energy. Warneck[23] has shown that, using the current notation, k_{MS}/k_{dSa} increases approximately exponentially with excitation energy above the dissociation threshold providing the basis of his algorithm for the acetone photodissociation quantum yield as a function of wavelength and pressure. The k_{MS}/k_{dSa} data in Tables 1 and 2 exhibit a similar dependence, although the decrease is less than exponential at the highest photolysis energies (Figure 6). Between 427 and 386 kJ mol^{-1} (280−310 nm) our data are in reasonable agreement with the end product data of Gierczak et al.[22] and of the Warneck group.[28,30] Their data are more scattered at longer wavelengths, where their end product methods required long photolysis times, with possible complications from secondary radical chemistry and interpretation via complex mechanisms. The LIF technique used here provides an improved approach at wavelengths beyond 310 nm. The main sources of error are the requirement of reproducible overlap of the photolysis and reference (248 nm) laser beams, drift in wavelength of the OH probe laser, and measurement of the energies of the photolysis lasers. Figure 7 shows a SV plot at 266 nm where the effect of quenching is small and hence the variation in ρ provides a realistic guide to the errors in the experimental method. The errors most probably arise from drift in the wavelength of the

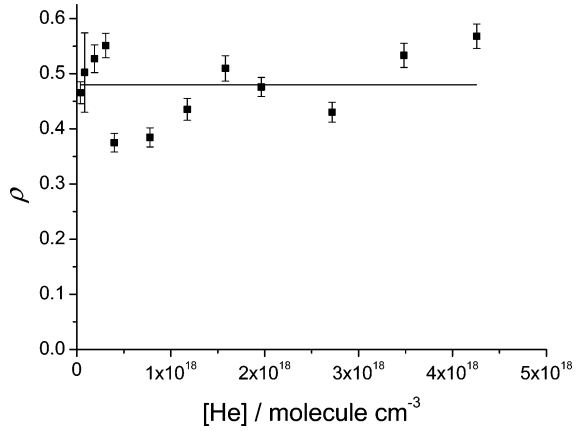

Figure 7. SV plot of the data at 266 nm and 248 K. At 266 nm, there is little quenching hence the variation in the plot provides a realistic guide to the errors in the experimental method. The average of the data is equal to 0.479 ± 0.063, where the error is equal to 2σ.

TABLE 3: Returned Parameters from Fitting the k_{MS}/k_{dSa} Data in Table 2 to eq E10[a]

wavelength/nm	A_{S1}/cm^3 molecule^{-1}	E_a/kJ mol^{-1}	B_{S1}/nm
302	$(2.84 \pm 1.18) \times 10^{-20}$	4.6 ± 0.8	299
305.5	$(1.41 \pm 1.28) \times 10^{-20}$	6.9 ± 1.8	300
308	$(1.21 \pm 0.82) \times 10^{-20}$	9.2 ± 1.4	301
310.5	$(3.2 \pm 2.8) \times 10^{-21}$	13.0 ± 1.8	300
312.5	$(9.3 \pm 8.2) \times 10^{-21}$	12.0 ± 1.8	303
315	$(9.5 \pm 2.6) \times 10^{-22}$	17.9 ± 0.6	301
317.5	$(3.1 \pm 2.2) \times 10^{-22}$	22.4 ± 1.4	300

[a] The data were weighted, and errors represent 2σ.

OH probe laser and measurement of the energies of the photolysis lasers.

While k_{MS}/k_{dSa} show an approximately exponential dependence over a wide range of excitation energies (Figure 6), the source of this dependence is not clear. Warneck ascribed it to an increase in k_{dSa} above the thermodynamic limit (338 nm [22]) for photolysis

$$(CH_3)_2CO + h\nu \rightarrow CH_3CO + CH_3 \qquad \text{(R1a)}$$

However, there is a wealth of evidence for a significant barrier on the S_1 surface[8,9,31] (see introduction), and the latest ab initio calculations from the Zewail group [32] have located the barrier at 259 nm, significantly above the S_1 origin at 328 nm,[33] see Figure 4. This dissociation occurs along the α-CC bond via a S_0/S_1 conical intersection and provides a route for dissociation on the S_0 surface. The wavelength dependence of k_{MS}/k_{dSa} is consistent with such a barrier on the S_1 surface.

Further evidence for a barrier on the singlet surface is reinforced from the temperature data in Table 2: k_{MS}/k_{dSa} has a positive temperature dependence which is more marked at longer wavelengths. Arrhenius plots were made for each set of k_{MS}/k_{dSa} at a given wavelength, and the results are summarized in Table 3. The results can be expressed in an empirical Arrhenius form

$$k_{MS}/k_{dSa} = A_{S1} \times \exp\left[\left(\frac{hc}{B_{S1}} - \frac{hc}{\lambda}\right)\frac{1}{kT}\right] \qquad \text{(E10)}$$

where $N_A hc(1/B_{S1} - 1/\lambda)$ is equal to the effective activation energy, E_a, and B_{S1} is the wavelength corresponding to the barrier maximum. Table 3 includes values for B_{S1}. Figure 8 is a plot of E_a vs $1/\lambda$, and its good linearity supports the validity of eq E10. The intercept with the $1/\lambda$ axis, 299 nm, is equal to B_{S1}, indicating together with the data in Table 3 that the barrier on the S_1 surface is located at ~300 nm. The origin of the dependence of the apparent A factor with wavelength (Table 3) is not clear.

TABLE 4: Returned Parameters from Fitting the k_{MT}/k_{dT} Data in Table 2 to eq E12[a]

wavelength/nm	A_{T1}/cm^3 molecule^{-1}	E_a/kJ mol^{-1}	B_{T1}/nm
305.5	$(1.5 \pm 15.0) \times 10^{-17}$	-2.7 ± 23.2	308 ± 20
308	$(9.4 \pm 25.4) \times 10^{-20}$	10.8 ± 5.4	300 ± 4
310.5	$(8.6 \pm 34.6) \times 10^{-19}$	9.1 ± 9.0	303 ± 7
312.5	$(2.3 \pm 7.8) \times 10^{-18}$	9.1 ± 6.8	305 ± 6
315.0	$(9.1 \pm 9.8) \times 10^{-18}$	6.6 ± 2.2	310 ± 2
317.5	$(1.6 \pm 1.0) \times 10^{-18}$	12.0 ± 1.2	308 ± 1

[a] The data were weighted, and errors represent 2σ.

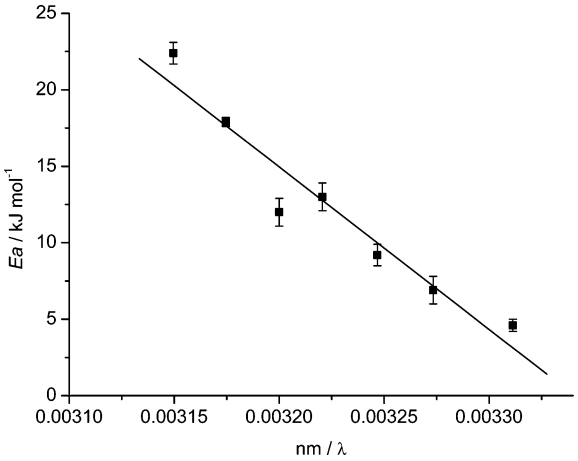

Figure 8. Plot of E_a vs $1/\lambda$ using the data in Table 3; see eq E10.

The use of eq E10 to describe the $k_{MS}/k_{dSa}(T)$ data is only a first approximation for two reasons: (i) The initial population in the S_1 state is not a Boltzmann distribution, the population is centered on the absorbing photon with a distribution that reflects the ground-state Boltzmann distribution, skewed to a small extent by Franck−Condon factors. (ii) It is assumed that k_{MS} is T independent. The effect of (ii) is reasonably expected to be small over the temperature range in this study as it is an energy transfer rate coefficient. A quantitative description of the system requires a master equation calculation using microscopic rate constants of the system together with an energy transfer model in order to give the observed macroscopic rate constant. Such calculations can be performed using any initial distribution. Such a calculation, incorporating the initial population in the S_1 state, is planned to model the k_{MS}/k_{dSa} parameters in order to assess the physical interpretation of eq E10 and the location of the barrier. A barrier corresponding to 259 nm has been proposed by Diau et al.[32]

***k_{ISC}/k_{dSa}* Parameter.** The determination of the ISC rate is facilitated by the differences in singlet and triplet lifetimes and the resulting change in slope in the SV plots. However, our measurements only determine rate coefficient ratios, and in Table 2, this ratio is given by k_{ISC}/k_{dSa}. To better observe the behavior of ISC with wavelength dividing the first two columns in Table 2 yields k_{ISC}/k_{MS}, where k_{MS} is the collisional rate constant for the quenching of S_1 which is reasonably assumed to show a weak dependence on wavelength. In the direct decay kinetics study of acetone by Copeland and Crosley,[29] a close to gas kinetic rate constant, k_{MT}, was measured for quenching by acetone and Ar of 1.3 and 0.3×10^{-10} cm^3 molecule^{-1} s^{-1}. Figure 9 is a plot of k_{ISC}/k_{MS} vs wavelength for 295 and 218 K, and within the scatter of the data, a "bell-shaped" curve can be discerned. In the acetone photolysis study by Emrich et al.,[28] a

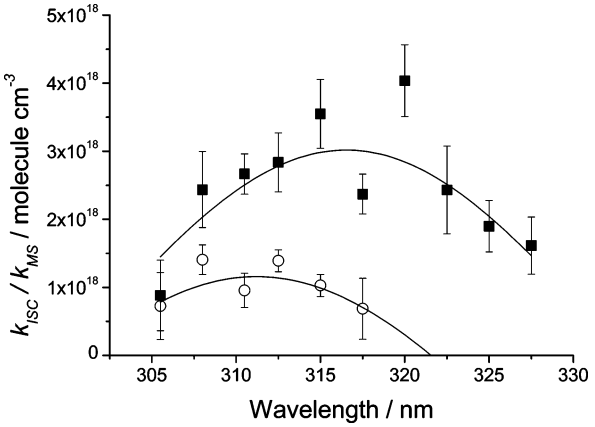

Figure 9. Plot of $k_{ISC}/k_{M,S}$ vs wavelength for the data at 295 K (■) and 218 K (○). The data appear to describe a "bell-shaped" function as demonstrated by the Gaussian fit to the data.

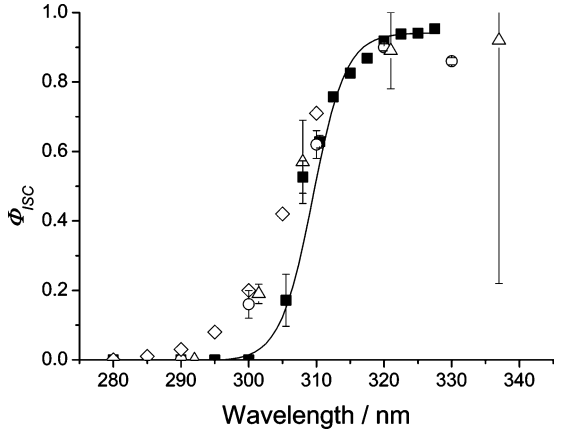

Figure 10. Plot of Φ_{ISC} vs wavelength for our 295 K data shown in Table 2, ■, together with the data from Warneck et al.,[23] ○, Gierczak et al.,[22] △, and Gandini et al.,[26] ◇, where the values at 13 Torr of acetone are used. The sigmoidal fit to our data is present to highlight the variation in all the data.

similar dependence for ISC was observed based on fits to k_{MS}/k_{dSa}. In the present study, the analysis is based on directly measured data.

The quantum yield for ISC at zero pressure is given by

$$\Phi_{ISC} = 1 - 1/[1 + (k_{ISC}/k_{dSa})] \qquad \text{(E11)}$$

A plot of Φ_{ISC} vs wavelength for our data in Table 2 together with the data from Gierczak et al.[22] Gandini and Hackett,[26] and Emrich and Warneck[28] is shown in Figure 10. Gandini et al.[26] measured Φ_{ISC} directly via sensitized phosphorescence; their data in Figure 10 refer to their lowest pressure (13.5 Torr CO_2). Over the range of 305−325 nm, all the data appear to be in fair agreement. Above 325 nm, Emrich et al.[28] observe a decrease in the Φ_{ISC} that is not observed in the other measurements; as noted above, the end product studies at these long wavelengths underestimate the effects of quenching. Figure 11 is plot of Φ_{ISC} vs wavelength using all our temperature data. This plot shows that Φ_{ISC} increases at shorter wavelengths as T is lowered and simply reflects the stronger temperature dependence of k_{dSa} compared with k_{ISC}.

Another feature of Figure 10 is that below 305 nm our Φ_{ISC} data appear to approach zero more quickly than those from the rest of the literature. Collision-induced ISC

$$S_1 + M \rightarrow T_1 + M \quad k_{ISC,M}$$

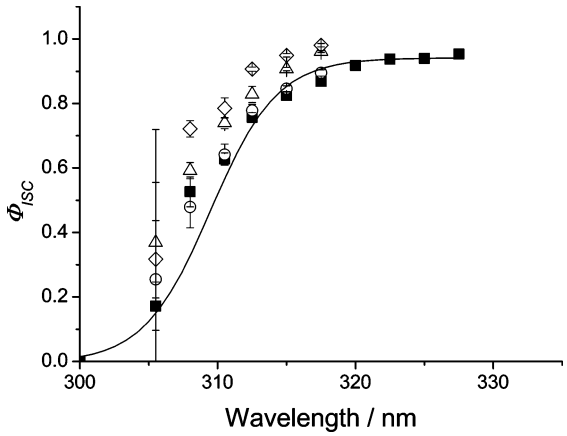

Figure 11. Temperature dependence of Φ_{ISC} vs wavelength using the data in Table 2: ■ = 295 K, ○ = 273 K, △ = 248 K, and ◇ = 218 K. The sigmoidal fit to the 295 K data is present to show the T dependence of the data.

provides a possible explanation and was proposed in the work by Gandini and Hackett.[26] The lowest pressure they used was 10 Torr of acetone, so that their higher ISC yields can be ascribed, at least partly, to collisional effects. They found that increasing the pressure of CO_2 substantially increased Φ_{ISC}, even at 250 nm. Collision-induced ISC does not compromise the current results, or interpretation, because T_1 is collisionally quenched much more rapidly than S_1.

From the "bell-shaped curve" for the dependence of k_{ISC} on wavelength, Figure 9, and the Φ_{ISC} vs wavelength data in Figure 10, there is the intriguing possibility that over a large wavelength range $k_{ISC} + k_{dSa}$ may be approximately constant; the decrease in k_{dSa} toward a longer wavelength is counterbalanced by the increase in k_{ISC}. Supporting evidence is provided by Breuer and Lee[11] who measured only a small change in the lifetime of singlet acetone with wavelength. Over the range of 313−280 nm the lifetime varies from 2.7 to 1.7 ns, and Heicklen[5] who found that Φ_F varies from 0.0021 to 0.0017 over the range 313−280 nm. These observations contradict the recent review by Haas[34] where ISC increases continuously with energy and it is stated that "ISC completely dominates the decay of S_1", based on the assumption that ISC will more efficiently couple S_1 to T_1 above its dissociation limit (∼305 nm).

***k_{MT}/k_{dT}* Parameter.** The triplet state quenching parameter, k_{MT}/k_{dT}, increases strongly with increasing wavelength and is at least an order of magnitude greater than quenching from the singlet, k_{MS}/k_{dSa}. This implies that information on the triplet can be observed only at low pressures, <25 Torr. Therefore, only direct emission studies[29,35−37] are able to be compared with our measurements. In the study by Copeland and Crosley,[29] an excitation-wavelength-independent quenching efficiency for the phosphorescence T_1 emission was observed over the wavelength range of 305−325 nm. The measured rate constants for acetone and Ar were 1.3 and 0.3 × 10^{-10} cm^3 $molecule^{-1}$ s^{-1}, respectively. The intercepts from these quenching plots yield values for k_{dT}, and though not reported, a value of ca. 10^5 s^{-1} is given from inspection. The ratio of these direct determinations is consistent with our k_{MT}/k_{dT} value of 2.73 × 10^{-16} cm^3 $molecule^{-1}$ at ∼320 nm; see Table 2. Also relevant to the present study, Greenblatt et al.[35] directly measured quenching of "hot" triplet acetone by He and O_2 and obtained the rate constants 3.6 and 7.8 × 10^{-10} cm^3 $molecule^{-1}$ s^{-1}, respectively. This small difference in quenching is consistent with the triplet quenching parameters, k_{MT}/k_{dT}, measured in the present study,

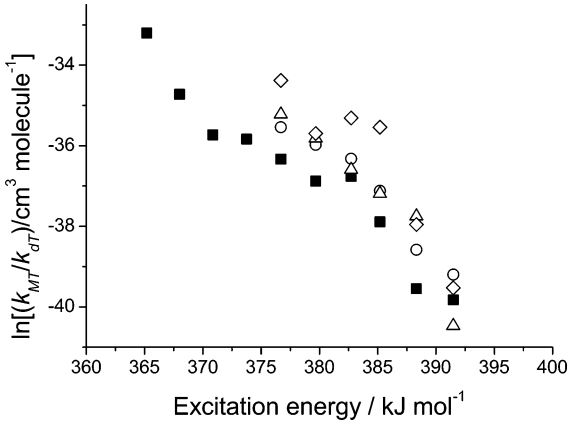

Figure 12. Plot of $\ln(k_{M,T}/k_{dT})$ vs excitation energy (photolysis wavelength) for our data: ■ = 295 K, ○ = 273 K, △ = 248 K, and ◇ = 218 K.

TABLE 5: Quantum Yield for CO, Φ_{CO}, at *RT*

wavelength/nm	Φ_{CO}	group
250	0.62	Leeds
	0.35	Gandini et al.[26]
	0.45	Meyrahn et al.[30]
265	0.37	Leeds
	0.18	Gandini et al.[26]
285	0.1	Horowitz [26,27]
	0.13	Leeds
	0.04	Gandini et al.[26]
300	0.06	Horowitz[26,27]
	0.04	Leeds
	0.03	Gandini et al.
	0.03	Meyrahn et al.[30]
313	0.03	Horowitz[26,27]
	0.012	Leeds
	∼0.0	Gandini et al.[26]
320	0.007	Leeds
	0.06	Meyrahn et al.[30]

which appear to suggest that the identity of the buffer gas has little effect on triplet quenching.

Figure 12 shows that k_{MT}/k_{dT} has an approximately exponential dependence on excitation energy, as is the case for the singlet quenching parameter. This behavior together with its temperature dependence is consistent with a barrier to dissociation on the triplet surface, and the returned parameters from Arrhenius fits to the data in Table 2 are summarized in Table 4. With the same assumptions as those used to derive eq 10, the barrier on the triplet surface, B_{T1}, is obtained from

$$k_{MT}/k_{dT} = A_{T1} \times \exp\left[\left(\frac{hc}{B_{T1}} - \frac{hc}{\lambda}\right)\frac{1}{kT}\right] \qquad \text{(E12)}$$

where $N_A hc(1/B_{T1} - 1/\lambda)$ is equal to the effective activation energy, E_a. Table 4 includes values obtained using this procedure for the barrier, B_{T1}. The data are of much lower precision than was the case for S_1. A reasonably consistent value of ∼306 nm is obtained for the location of the barrier to dissociation on the triplet surface. This value is in agreement with the analysis of Copeland and Crosley,[29] where the rapid reduction in emission below this wavelength was assigned as the onset of dissociation. A more accurate value was obtained from the emission studies by Zuckermann et al.[4] where acetone was seeded in a supersonic molecular beam. The cooled acetone in these experiments showed a rapid decrease in the emission lifetime, equivalent to emission loss with respect to dissociation, at 305.7 nm. Therefore, it appears that the present results are able to reliably locate the barrier for dissociation on the triplet surface. The quenching parameters, k_{MT}/k_{dT}, are too high for T_1 to contribute significantly to acetone photolysis in the atmosphere.

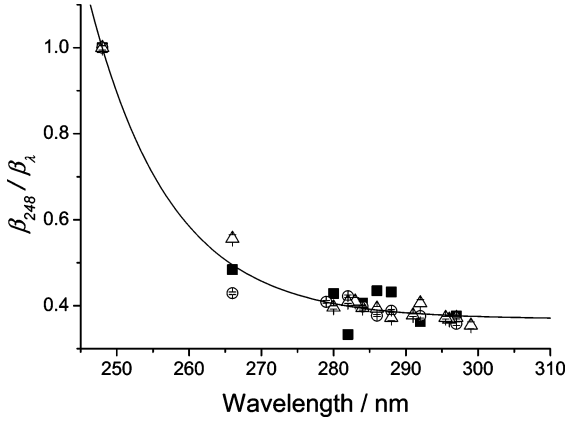

Figure 13. Intercepts, $\beta_{248}/\beta_\lambda$, of all the data at *RT* plotted vs wavelength: ■ = N_2, ○ = air, and △ = He. The solid line represents an exponential fit using eq E12 to the data.

(c) $(CH_3)_2CO \rightarrow 2CH_3 + CO$, the $\beta_{248}/\beta_\lambda$ Parameter. From the intercept data, $\beta_{248}/\beta_\lambda$, in Table 1 and eq E4, it is evident that the zero pressure yield of CH_3CO at 248 nm is less than that at the longer wavelengths. Figure 1 shows at the lowest pressure, the OH yield from acetyl at 308 nm is greater than that at 248 nm. It has been established that at shorter wavelengths the mechanism for acetone photolysis switches from two-body photolysis, generating $CH_3CO + CO$ (R1a), to three-body photolysis, generating $2CH_3 + CO$ (R1b).[12,23,26,27] At 248 nm, both channels are known to operate.[12] The zero pressure intercept data in Table 1 demonstrate that both photolysis channels, R1a and R1b, operate at 248 nm. Figure 13 shows a plot of $\beta_{248}/\beta_\lambda$ vs λ. The thermodynamic limit for R1b is 300 nm. The data show that $\beta_{248}/\beta_\lambda$ decreases from unity at 248 nm to a limit of 0.37 for $\lambda \geq 300$ nm implying a fractional yield of R1b at 248 nm of 0.63 and a decrease in this yield to zero at 300 nm.

The dependence of $\beta_{248}/\beta_\lambda$ on wavelength is adequately described by the exponential relationship

$$1 + p(1 - q\exp(\lambda/\text{nm} - 248)) \quad (\lambda \geq 248\ \text{nm}) \qquad \text{(E13)}$$

These fitting parameters were adjusted to best fit all the 295 K intercept data in Table 1, with the data assigned an equal weighting. The fit to the data is shown by the solid line in Figure 13 and is expressed by the following parameters: $q = 0.089 \pm 0.01$ and $p = 0.37 \pm 0.01$. p is equal to β_{248}, the zero pressure quantum yield for CH_3CO at 248 nm, $\Phi_{CH3CO,248,M=0}$.

The zero pressure CO quantum yield, Φ_{CO}, is equal to $1 - \Phi_{CH3CO,\lambda,M=0}$

$$\Phi_{CO,\lambda} = 1 - \Phi_{CH3CO,\lambda,M=0} = 1 - \left(\beta_{248} \times \frac{\beta_\lambda}{\beta_{248}}\right) \qquad \text{(E14)}$$

where β_{248} is equal to p in eq E13 and $(\beta_{248}/\beta_\lambda)$ is equal to the intercept in Table 1. Φ_{CO} is shown in Table 5, together with data from previous determinations.[26,27] While there is considerable spread in Φ_{CO}, the trend with wavelength appears to be consistent over the range of 250−300 nm. However, at wavelengths above 300 nm, there appears a distinct deviation in the data: our data and that of Gandini et al. show Φ_{CO} to be rapidly falling away, but the measurements of Horowitz[27] and Meyrahn et al. show a less dramatic dependence. Our measure-

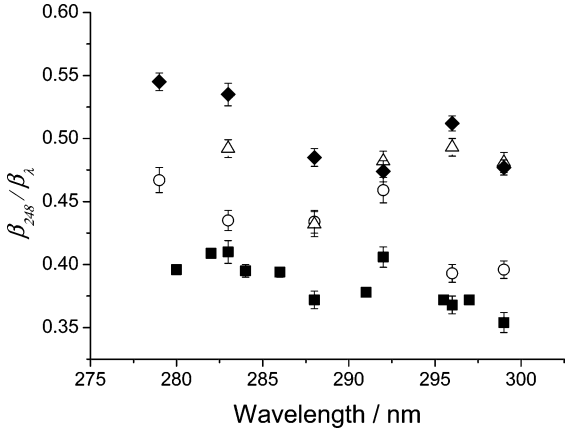

Figure 14. Plots of the He intercept data, $\beta_{248}/\beta_\lambda$, over the wavelength range of 275−300 nm at various temperatures: ■ = 295 K, ○ = 273 K, ▲ = 248 K, and ◆ = 218 K. The plots show that the intercepts are increasing as the temperature is lowered.

ments directly monitored the products of acetone photolysis in time and Gandini et al.[26] directly monitored the CO in the steady-state photolysis of acetone, but the experiments of Horowitz[27] and Meyrahn[30] were indirect studies where additional chemicals were added to the system in order to form stable, identifiable products. Therefore, it is reasonable to conclude that the direct studies of the system yield more reliable values for Φ_{CO}. In addition, it should be borne in mind that the reduced absorption cross-section for acetone above 300 nm[22] is such that acetone was photolyzed for a greatly increased time. Recently, Emrich et al.[28] used the literature data to determine a parametrized expression for Φ_{CO}, but used data that were weighted toward the indirect studies; consequently, we suggest our above expression for Φ_{CO} at 295 K is more reliable.

North et al.[18] using the technique of photofragment translation spectroscopy obtained a value of 0.30 ± 0.04 for Φ_{CO} at 248 nm, which would appear to be in major disagreement with our measurement, $\Phi_{CO} = 0.63$. However, it is noted that the measurements of North et al.[18] were made in a molecular beam, where the temperature of the acetone is very low, and it is this difference in temperature between the two measurements that is the most probable source of the discrepancy in the Φ_{CO} values, that is, there is a barrier to dissociation. From the data in Table 1, a plot of the He intercept data vs wavelength provides evidence for Φ_{CO} being temperature dependent. Figure 14 is a plot of the He intercept data, $\beta_{248}/\beta_\lambda$, over the wavelength range of 275−300 nm showing that the values of the intercept ratio increase as the temperature is lowered. This effect reflects the temperature dependence of Φ_{CO}, which can be quantified by assigning a LT^n dependence to the parameters in eq E13, that is

$$q = q_1(T/295)^{q2} \qquad \text{(E13a)}$$

$$p = p_1(\mathrm{T}/295)^{p2} \qquad \text{(E13b)}$$

All the He intercept data in Table 1 were fitted, with weighting, to this extended form of eq E13. The returned parameters are listed in Table 6. Extrapolating to $T \sim 110$ K, Φ_{CO} at 248 nm is equal to the value of North et al.[12] While it is acknowledged that this extrapolation of the data is associated with considerable uncertainty, it does indicate a T for acetone that is consistent with a lower vibrational T expected in molecular beam studies. Another apparent discrepancy regarding Φ_{CO} comes from a separate photofragment translation spectroscopy study at 266 nm where no CO was observed under molecular beam conditions.[19] This contrasts with our study where our 295 K data, using the parameters from eqs E13 and E14, indicate that 0.37 of the photolysis at 266 nm is producing CO. But this difference in Φ_{CO} is again reflecting the T dependence of Φ_{CO}; this photofragment translation spectroscopy experiment was done in a molecular beam where the T value is low. In fact, the temperature dependence from our data suggests that below 225 K essentially no CO is produced at 266 nm.

TABLE 6: Returned Parameters from a Fitting of eq E13 to the He Intercept Data in Table 1

	L	n
$q = q_1\,(T/295)^{q2}$	0.0865 ± 0.006	−4.6 ± 1.6
$p = p_1\,(T/295)^{p2}$	0.369 ± 0.004	−1.07 ± 0.06

[a] The data was weighted, and errors represent 2σ.

The origin of the wavelength and temperature dependence of Φ_{CO} is related to the stepwise nature of R1b involving $CH_3CO^* \rightarrow CH_3 + CO$. The thermal reaction has a barrier of 71 ± 4 kJ mol^{-1}.[18,38] The photofragment translation spectroscopy experiment of Waits et al.[19] at 266 nm determined that the nascent acetyl radical has 57 kJ mol^{-1} of internal energy, which is insufficient to surmount the barrier for dissociation. This implies that a minimum of 71−57 = 14 kJ mol^{-1} extra energy is required for the three-body dissociation. However, it is more likely that even more energy is required to bring about a three-body photodissociation because the extra energy might go into translation of CH_3CO and CH_3 fragments and not internal energy.

Finally, in this section, it should be emphasized that these values for Φ_{CO} were obtained from $1 - \Phi_{CH3CO,M=0}$, the zero pressure CH_3CO quantum yield, via the extrapolation of SV plots to zero pressure, whereas the photofragment translation spectroscopy experiments are performed under collision free conditions. If CO is formed exclusively from S_1, see photolysis model in section 5, then the CO yield will be pressure quenched in the same way as CH_3CO. However, the results of Gandini et al. and Horowitz [26,27] imply that the CO yield is independent of total pressure, so that collisions have no influence on reaction R1b. Recently, this pressure independence of the CO yield has been questioned in the work by Somnitz et al.[39] In this end product study, acetone was photolyzed at 248 nm in the presence of N_2 before being transferred to an absorption cell which measured CO. The CO yield was observed to decrease from 0.45 at 15 Torr to 0.25 at 680 Torr. This effect was attributed to the stabilization of energized CH_3CO (rate constant, k_{stab}), which in the absence of collisions dissociates to CO + CH_3 (rate constant, k_{diss}). To assess the impact of this effect on our present results, we have analyzed their data using a simple quenching model and obtained a quenching parameter, k_{stab}/k_{diss}, equal to $\sim 3 \times 10^{-20}$ cm^3 molecule^{-1}. Reanalysis of some of our data including this pressure dependence at 248 nm returned lower values of k_{MS}/k_{dSa} than those shown in Table 1. Within the quality of our data, however, we are unable to discern if this energized CH_3CO pressure quenching is present. The fit to the data is not improved by the inclusion of this additional feature, but equally it is not ruled out.

This pressure-dependent CO yield at 248 nm observed by Somnitz et al.[39] is in disagreement with previous investigations.[22,26−28] In particular, Gandini and Hackett,[26] using a sensitive CO detection system, found no pressure dependence in the CO yield from acetone photolysis when studied over a greater range of pressures (13.5−885 Torr) and wavelengths (250−330 nm). They also determined the yield of acetyl by

measuring its recombination product, biacetyl. The mechanism developed in section 5 is based on the Gandini and Hackett results and assumes that CO is formed from S_1*, which dissociates too quickly to be collisonally stabilized.

If the pressure dependence of the CO yield is incorporated in our analysis, then the effect is quite marked at wavelengths below 300 nm, reducing the quenching parameter k_{MS}/k_{dSa}, because of the increase in the yield of acetyl at 248 nm, by a factor of 2−3. The effect becomes less significant above 300 nm, because the longer S_1 lifetime leads to an increase in k_{MS}/k_{dSa}, which is now reduced by ≤15% when the CO pressure dependence is incorporated. This reduction in the rate coefficient ratio becomes even less important as the wavelength is increased. Thus, the effects of any pressure dependence in the 248 nm CO yield at atmospherically significant wavelengths are negligible.

7. Mechanism for Acetone Photolysis and Quenching

The proposed photolysis mechanism was developed in section 5. It is based on decomposition from the S_1 and T_1 states, with wavelength thresholds of 300 and 306 nm, respectively. Both states are collisionally quenched leading to a reduction in the photolysis yield.

Cundall and Davies, using 313.0 and 253.7 nm excitation, and O'Neal and Larson,[40] using 313.0 nm excitation, both observed a quenchable and a nonquenchable contribution to the acetone photolysis yield. Cundall and Davies attributed this behavior to involvement from the S_1 (nonquenchable) and the T_1 (quenchable). However, O'Neal and Larson put forward a different explanation [41] based on the rapid ISC from S_1 to a highly excited triplet, T_1**. They suggested that this state can either dissociate or relax via collisions to a thermally equilibrated triplet, T_1, which can be thermally activated to energies above the dissociation barrier. This latter mechanism has prevailed in recent years supported by correlation diagrams and ab initio calculations,[9,17] which fail to predict a low-energy pathway to dissociation on S_1. This model has recently been reviewed by Haas[34] and is used to describe the extensive time-resolved acetone emission studies from the Haas group.[4,34−36]

Breuer and Lee[11] measured a singlet lifetime of 2.7−1.7 ns, over the wavelength range 313−280 nm, in single-photon counting experiments. The present experiments only give SV slopes, which correspond to the ratio of the quenching rate coefficient to the reciprocal lifetime of the S_1 or T_1 states. The quenching rate coefficients change little with quencher, suggesting they are large. Taking a wavelength-independent quenching rate coefficient for He of 3×10^{-11} cm^3 molcule^{-1} s^{-1} gives an S_1 lifetime of ∼2 ns at wavelengths below 300 nm, from the data in Table 1, assuming the mechanism in section 5.

A sub 10 ns emission was observed by Haas and coworkers[4,35−37,42] and assigned to dephasing of the wave packet out of the Franck−Condon region on the S_1 surface. This dephasing process has recently been measured in various femtosecond pump probe experiments[15,16,32] and is observed to occur in less than 200 fs. Owrutsky et al.[16] and Zhong et al.[15] suggested that this fast femtosecond loss is dissociation, but the more recent femtosecond/theoretical study by Diau et al.[32] shows that dissociation is highly unlikely. Such a rapid dissociation would give a quantum yield for fluorescence, Φ_F, of $\sim 2 \times 10^{-8}$ which is 5 orders smaller than the measured yield of 0.0021−0.0017 over the range of 313−280 nm.[5]

ISC becomes significant above 300 nm, based on the observation of the nonlinear SV slopes presented here. The ratio of the two intercepts of the SV plots gives the ratio of the ISC to dissociation rate constants (eq E8). Once again, assuming a wavelength-independent quenching rate coefficient for He of 3×10^{-11} cm^3 molcule^{-1} s^{-1} gives an S_1 lifetime at 295 K that increases from ∼6 ns at 302 nm to ∼20 ns at 327.5 nm; in this range, the lifetimes $(k_{ISC} + k_{dSa})^{-1}$ are equal (since k_F is very small). This comparatively small change in lifetime occurs over a wavelength range in which the dissociation rate constant decreases by a factor of 70, demonstrating the compensation arising from ISC and supporting the suggestion made in section 6 that there is a tradeoff between ISC and dissociation. At the longest wavelength, 327.5 nm, and lowest pressures, we observed emission from acetone having a lifetime longer than the 10 ns laser probe pulse. At this wavelength in the molecular beam experiments of Zuckermann et al.,[4] the sub 10 ns emission is not present.

Copeland and Crosley[29] observed emission from T_1, following excitation between 305 and 325 nm, with two distinct lifetimes of ∼15 and ∼225 μs which were assigned to "hot" and thermal triplet phosphorescence, respectively. They also determined a rate constant for quenching by Ar of 3×10^{-11} cm^3 molcule^{-1} s^{-1}. Assuming the same value for He, this gives 295 K triplet lifetimes increasing from 170 ns at 305 nm to 30 μs at 327.5 nm. Decreasing the He rate constants leads, of course, to longer estimates for the lifetime.

The mechanism of such a rapid quenching of the singlet and triplet states by an inert gas and the similarity of the S_1 quenching rate constants for He, N_2, and O_2 is not clear. The most likely mechanism is collisional deactivation of the vibrationally excited S_1 and T_1 states coupled with an energy-dependent rate of dissociation, which in turn is compatible with the temperature dependence of the dissociation rate constant. The suggested rate constant for He quenching is compatible with such a mechanism. Collisional efficiencies of 0.1−0.2 are widely used in the field of thermal unimolecular dissociation.[43,44] This suggestion is being tested via master equation calculations.

8. Atmospheric Implications

Acetone photolysis can act as a source of OH and HO_2 radicals and peroxyacetylnitrate (PAN) following reactions of CH_3CO and CH_3 photofragments in the atmosphere. For acetone, the reaction with OH and photolysis are the two major loss mechanisms in the atmosphere. The effect of increasing altitude on acetone loss is 2-fold: first, the lower temperature switches off the reaction between OH and acetone in favor of the photolysis, which compared to the reaction has a greater HO_x creating potential,[21] and second, HO_x production from ozone photolysis is rapidly diminished as water vapor concentration decreases in the UT. Hence, models have indicated that acetone photolysis is an important HO_x source in the upper troposphere (UT).[45] All the models to date have used *T*-independent acetone photolysis quantum yields, $\Phi_{total}(\lambda,[M])$, based on the gas chromatography data from Gierczak et al.[22] and Warneck.[23] However, the results of this direct measurement study show that the effects of acetone quenching are enhanced beyond 310 nm, the difference dramatically increasing at even longer wavelengths. In addition, over this wavelength range, there is a *T* dependence that makes quenching even more pronounced at low *T* values. For wavelengths >290 nm, the solar flux is increasing exponentially,[46] and hence, although the quantum yields are small, any changes make a significant difference to the atmospheric acetone budget. Smaller photolysis quantum yields imply that the lifetime of acetone is longer.

We recently published papers[47,48] on the parametrization of the quantum yield data in Tables 1 and 2[48] and showed the

impact of these temperature-dependent quantum yields, $\Phi_{total}(\lambda,[M],T)$, on the chemistry in the UT.[47] Therefore, in this section, we only summarize the results from these papers together with details that were omitted due to space requirements. The total acetone photolysis quantum yield is given by

$$\Phi_{total}(\lambda,[M],T) = \Phi_{CH3CO}(\lambda,[M],T) + \Phi_{CO}(\lambda,T) \qquad (E15)$$

From the above equation, $\Phi_{CO}(\lambda,T)$ is given by eqs E13 and E14 and $\Phi_{CH3CO}(\lambda,[M],T)$ is given by (E13/E5) $\times$ $[1 - \Phi_{CO}(\lambda,T)]$; see eq E16 below. In the above section 6c, an expression for $\Phi_{CO}(\lambda,T)$ was determined by fitting eq E13 to the data in Table 1; the parameters are given in Table 6. In our recent paper,[48] the reported parameters for $\Phi_{CO}(\lambda, T)$ were derived from fitting directly to the $[CH_3CO]_{0,248}/[CH_3CO]_{0,\lambda}$ data; the difference between the parameters in Table 6 and our recent paper[48] are within error and not significant. In the UT, solar flux is dramatically increasing above 300 nm but this is where the contribution from $\Phi_{CO}(\lambda,T)$ is negligible; see Table 6. Therefore, for tropospheric modeling, the second term in eq E15 can be reasonably ignored, Φ_{CO}(300 nm, 295 K) $\sim$ 0.02.

$\Phi_{CH3CO}(\lambda, [M], T)$ is given by (E13/E5) $\times$ $[1 - \Phi_{CO}(\lambda,T)]$ and is equal to

$$\frac{1 + \frac{k_{MT}}{k_{dT}}[M] + \frac{k_{ISC}}{k_{dSa}}}{\left(1 + \frac{k_{MS}}{k_{dSa}}[M] + \frac{k_{ISC}}{k_{dSa}}\right)\left(1 + \frac{k_{MT}}{k_{dT}}[M]\right)} \times [1 - \Phi_{CO}(\lambda,T)] \qquad (E16)$$

From Figure 6, it is observed that k_{MS}/k_{dSa} show an exponential dependence over a significant range but not over the entire 266−327.5 nm range. We overcome this by dividing the range into two, using 302 nm as the crossover point. The 302 nm crossover point is chosen, in part, because below this wavelength the above equation reduces to a simple SV relationship described just by k_{MS}/k_{dSa}. Therefore, only the k_{MS}/k_{dSa} parameter is described over two ranges. Over the range of 279−302 nm, the k_{MS}/k_{dSa} ratio was best modeled by the exponential equation

$$\frac{k_{MS}}{k_{dS}} = a \exp\left(-b\left\{\frac{10^7}{\lambda} - 33113\right\}\right) \qquad (E17)$$

where $a = (1.576 \pm 0.062) \times 10^{-19}$ $(T/295)^{(-2.4\pm0.16)}$ and $b = (5.4 \pm 0.04)$ $(T/295)^{(-3.280\pm0.26)}$; these fitting parameters were derived from fitting directly to the $[CH_3CO]_{0,248}/[CH_3CO]_{0,\lambda}$ data. In eq E17, 33113 is equal (in cm^{-1}) to the 302 nm limit for which this equation is valid.

Over the range of 302−327.5 nm, the k_{MS}/k_{dSa} and k_{MT}/k_{dT} data are well described by an exponential—see Figures 6 and 11—and are best modeled by the equations

$$\frac{k_{MS}}{k_{dSa}} = a_1 \exp\left(-b_1\left\{\frac{10^7}{\lambda} - 30488\right\}\right) \qquad (E18)$$

$$\frac{k_{MT}}{k_{dT}} = a_3 \exp\left(-b_3\left\{\frac{10^7}{\lambda} - 30488\right\}\right) \qquad (E19)$$

In eqs E18 and E19, 30488 is equal (in cm^{-1}) to the S_1 origin at 328 nm.[33] The "bell-shaped curve" for ISC—see Figure 9—means that it is best described by a Gaussian, and consequently, the ratio k_{ISC}/k_{dSa} was modeled by the equation

$$\frac{k_{ISC}}{k_{dSa}} = a_2 \exp\left(-b_2\left\{\frac{10^7}{\lambda} - c_2\right\}^2\right) \qquad (E20)$$

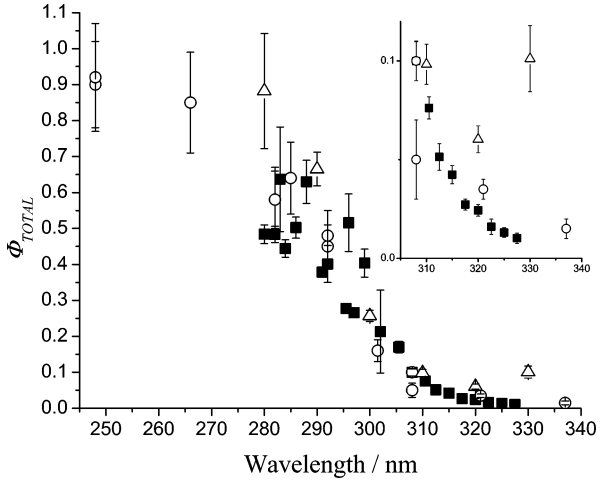

Figure 15. Wavelength dependence of the total quantum yield, Φ_{total}, at 1 atm and 295 K determined in this work (■), Gierczak et al.[22] (○), and Emrich et al.[28] (△). Our yields are determined by extrapolation of the fits to individual SV plots and not from parametrizations. The inset shows a blow-up of the region $\lambda > 305$ nm.

Equations E18−20 were inserted in eq E5, which were then used to simultaneously fit to all the $[CH_3CO]_{0,248}/[CH_3CO]_{0,\lambda}$ data: eq E13 was used to describe $(\beta_{248}/\beta_\lambda)$ and was fixed to the parameters given in Table 6. The returned parameters are as follows: $a_1 = (1.61 \pm 0.12) \times 10^{-17}$ $(T/295)^{(-10.04\pm0.40)}$ and $b_1 = (1.79 \pm 0.04) \times 10^{-3}$ $(T/295)^{(-1.363\pm0.072)}$; $a_2 = (25.51 \pm 1.68)$ $(T/295)^{(-6.62\pm0.46)}$ $b_2 = (5.811 \pm 0.40) \times 10^{-7}$ $(T/295)^{(-2.90\pm0.18)}$, $c_2 = (30031 \pm 80)$ $(T/295)^{(-0.062\pm0.006)}$; $a_3 = (1.66 \pm 0.28) \times 10^{-15}$ $(T/295)^{(-7.21\pm1.08)}$ and $b_3 = (2.09 \pm 0.14) \times 10^{-3}$ $(T/295)^{(-1.141\pm0.30)}$. The quoted errors are 2σ, and the units in these fitting expressions are [M] = molecule cm^{-3}, λ = nm, and T = K.

The above expressions allow $\Phi_{total}(\lambda,[M],T)$ to be evaluated, but it is noted that there is a slight discontinuity in the parametrized curve at 302 nm, which is caused by the switch over in the k_{MS}/k_{dSa} expression at this wavelength. However, as noted above for $\Phi_{CO}(\lambda,T)$, in the UT, the dependence of solar flux with wavelength is such that $\lambda < 300$ nm contributes little to acetone photolysis. Therefore, using only the equations that describe the high wavelength range adequately describe $\Phi_{total}(\lambda,[M],T)$ in the UT. In Figure 15, the values for $\Phi_{total}(\lambda,[M],T)$ at 1 atm and 295 K determined in this work are compared to the end product studies of Gierczak et al.[22] and Emrich et al.[28] This plot shows that there is fair agreement up to $\sim$320 nm, but beyond this wavelength, our data show significantly smaller yields for acetone photolysis. Moreover, our data show there is a large T dependence—see Table 2—that makes the difference even larger at lower T.

The rate of photolysis of acetone is given by

$$J = \int_\lambda \sigma(\lambda,T)\phi_{total}(\lambda,[M],T)F(\lambda,z,\chi)\,d\lambda \qquad (E21)$$

where F is the actinic photon flux that depends on wavelength, λ, altitude, z, and solar zenith angle, χ, and $\sigma(\lambda,T)$ is the absorption cross-section of acetone. To quantify the effect our values for $\Phi_{total}(\lambda,[M],T)$ have on the rate of acetone photolysis, J(new), compared to the presently IUPAC recommended values

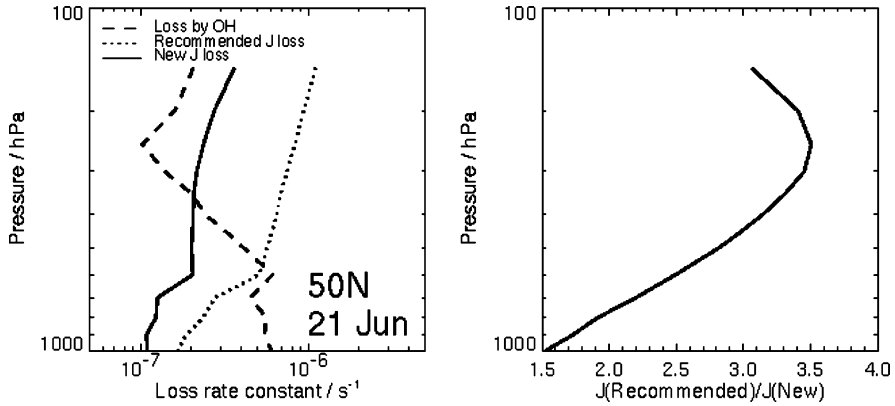

Figure 16. Left: rate of loss of acetone by photolysis and reaction with OH calculated as a function of altitude for 21 June at 50° N. Right: ratio *J*(recommended)/*J*(new). See text for details.

for $\Phi_{total}(\lambda,[M])$, used to calculate *J*(recommended), and based on the work of Gierczak and Warneck, the CiTTyCAT box model[49] has been run as a function of altitude for 21 June at 50° N. The results are shown in Figure 16, where our $\Phi_{total}(\lambda,[M],T)$ values produce averaged photolysis rates that are lower than the recommended at all altitudes reaching a factor of 3.5 lower in the UT/lower stratosphere region. This effect is mainly due to temperature-dependent changes in $\Phi_{total}(\lambda,[M],T)$, and when the box model was run in mid-winter (21 December) at 50° N, a maximum factor of *J*(recommended)/*J*(new) = 10 was observed for the UT. More details on these calculations and the atmospheric implications can be found in our recently published papers.[47,48]

9. Conclusions

The present study used a laser photolysis/LIF technique to detect radicals produced from acetone photolysis. The LIF detection provides a highly sensitive relative measure of the photolysis yields, which were placed on an absolute basis by comparing the yield at various photolysis wavelengths to the 248 nm reference wavelength, where the total acetone photodissociation yield is 100%. This is the first time-resolved determination of the quantum yield for acetone photolysis, $\Phi_{total}(\lambda,[M],T)$. In general, pressure quenching of the dissociating states increases with wavelength over the range of 266−327.5 nm, and above ∼300 nm, pressure quenching showed a systematically increasing temperature dependence over the range of 295−218 K; this *T* dependence has not been previously observed. Stern−Volmer analysis of the data reveals linear behavior below 300 nm and nonlinear behavior above 300 nm. This behavior requires dissociation from at least two excited states, and we have developed a photolysis model where at short wavelengths, $\lambda < 300$ nm, dissociation is occurring exclusively via the excited singlet, S_1, and at long wavelengths, $\lambda > 300$ nm, dissociation is occurring via both the excited singlet, S_1, and the excited triplet, T_1. Barriers to dissociation are invoked in order to explain the dependence of pressure quenching of the acetone photolysis yields as a function of wavelength and temperature. This photolysis model is shown to return rational parameters when fitting the data and also can be used to adequately describe the literature. A parametrized expression for $\Phi_{total}(\lambda,[M],T)$ has been developed and when incorporated into a box model simulation of the atmosphere reveals that the acetone photolysis yield is much less than that when using the currently recommended $\Phi_{total}(\lambda,[M])$, especially for the upper troposphere. The implication is a longer atmospheric lifetime for acetone.

Acknowledgment. M.A.B., D.E.H., and M.J.P. thank the NERC UTLS-03 Ozone Program (Award GST/02/2428) for funding this work. Thanks are given to Steve R. Arnold and Martin P. Chipperfield for their assistance in running the CiTTyCAT box model[49] calculation of Figure 16.

References and Notes

(1) Hansen, D. A.; Lee, E. K. C. *J. Chem. Phys.* **1975**, *62*, 183.
(2) Anner, O.; Zuckermann, H.; Haas, Y. *J. Phys. Chem.* **1985**, *89*, 1336.
(3) Zuckermann, H.; Schmitz, B.; Haas, Y. *Chem. Phys. Lett.* **1988**, *151*, 323.
(4) Zuckermann, H.; Schmitz, B.; Haas, Y. *J. Phys. Chem.* **1989**, *93*, 4083.
(5) Heicklen, J. *J. Am. Chem. Soc.* **1959**, *81*, 3863.
(6) Thurber, M. C.; Hanson, R. K. *Exp. Fluids* **2001**, *30*, 93.
(7) Thurber, M. C.; Hanson, R. K. *Appl. Phys. B: Lasers Opt.* **1999**, *69*, 229.
(8) Turro, N. J.; Farneth, W. E.; Devaquet, A. *J. Am. Chem. Soc.* **1976**, *98*, 7425.
(9) Liu, D.; Fang, W. H.; Fu, X. Y. *Chem. Phys. Lett.* **2000**, *325*, 86.
(10) Zuckermann, H.; Schmitz, B.; Haas, Y. *J. Phys. Chem.* **1988**, *92*, 4835.
(11) Breuer, G. M.; Lee, E. K. C. *J. Phys. Chem.* **1971**, *75*, 989.
(12) North, S. W.; Blank, D. A.; Gezelter, J. D.; Longfellow, C. A.; Lee, Y. T. *J. Chem. Phys.* **1995**, *102*, 4447.
(13) Shibata, T.; Suzuki, T. *Chem. Phys. Lett.* **1996**, *262*, 115.
(14) Buzza, S. A.; Snyder, E. M.; Castleman, A. W., Jr. *J. Chem. Phys.* **1996**, *104*, 5040.
(15) Zhong, Q.; Poth, L.; Castleman, A. W., Jr. *J. Chem. Phys.* **1999**, *110*, 192.
(16) Owrutsky, J. C.; Baronavski, A. P. *J. Chem. Phys.* **1998**, *108*, 6652.
(17) Sakurai, H.; Kato, S. *THEOCHEM* **1999**, *461*−*462*, 145.
(18) North, S.; Blank, D. A.; Lee, Y. T. *Chem. Phys. Lett.* **1994**, *224*, 38.
(19) Waits, L. D.; Horwitz, R. J.; Guest, J. A. *Chem. Phys.* **1991**, *155*, 149.
(20) Singh, H. B.; Ohara, D.; Herlth, D.; Sachse, W.; Blake, D. R.; Bradshaw, J. D.; Kanakidou, M.; Crutzen, P. J. *J. Geophys. Res., [Atmos.]* **1994**, *99*, 1805.
(21) Singh, H. B.; Kanakidou, M.; Crutzen, P. J.; Jacob, D. J. *Nature* **1995**, *378*, 50.
(22) Gierczak, T.; Burkholder, J. B.; Bauerle, S.; Ravishankara, A. R. *Chem. Phys.* **1998**, *231*, 229.
(23) Warneck, P. *Atmos. Environ.* **2001**, *35*, 5773.
(24) Blitz, M. A.; Heard, D. E.; Pilling, M. J. *Chem. Phys. Lett.* **2002**, *365*, 374.
(25) Aloisio, S.; Francisco, J. S. *Chem. Phys. Lett.* **2000**, *329*, 179.
(26) Gandini, A.; Hackett, P. A. *J. Am. Chem. Soc.* **1977**, *99*, 6195.
(27) Horowitz, A. *J. Phys. Chem.* **1991**, *95*, 10816.
(28) Emrich, M.; Warneck, P. *J. Phys. Chem. A* **2000**, *104*, 9436.
(29) Copeland, R. A.; Crosley, D. R. *Chem. Phys. Lett.* **1985**, *115*, 362.
(30) Meyrahn, H.; Pauly, J.; Schneider, W.; Warneck, P. *J. Atmos. Chem.* **1986**, *4*, 277.
(31) Salem, L. *J. Am. Chem. Soc.* **1974**, *96*, 3486.
(32) Diau, E. W. G.; Kotting, C.; Zewail, A. H. *ChemPhysChem* **2001**, *2*, 294.
(33) Baba, M.; Hanazaki, I.; Nagashima, U. *J. Chem. Phys.* **1985**, *82*, 3938.

(34) Haas, Y. *Photochem. Photobiol. Sci.* **2004**, *3*, 6.
(35) Greenblatt, G. D.; Ruhman, S.; Haas, Y. *Chem. Phys. Lett.* **1984**, *112*, 200.
(36) Haas, Y. *Spectrochim. Acta, Part A* **1990**, *46*, 541.
(37) Haas, Y.; Zuckermann, H. *Isr. J. Chem.* **1989**, *29*, 405.
(38) Watkins, K. W.; Word, W. W. *Int. J. Chem. Kinet.* **1974**, *6*, 855.
(39) Somnitz, H.; Fida, M.; Ufer, T.; Zellner, R. *Phys. Chem. Chem. Phys.* **2005**, *7*, 3342.
(40) Larson, C. W.; O'Neal, H. E. *J. Phys. Chem.* **1966**, *70*, 2475.
(41) O'Neal, H. E.; Larson, C. W. *J. Phys. Chem.* **1969**, *73*, 1011.
(42) Zuckermann, H.; Haas, Y.; Drabbels, M.; Heinze, J.; Meerts, W. L.; Reuss, J.; Van Bladel, J. *Chem. Phys.* **1992**, *163*, 193.
(43) Troe, J. *Ber. Bunsen-Ges. Phys. Chem.* **1974**, *78*, 478.
(44) Holbrook, K. A.; Pilling, M. J.; Robertson, S. H. *Unimolecular Reactions*, 2nd ed.; Wiley: New York, 1996.
(45) Jaegle, L.; Jacob, D. J.; Brune, W. H.; Wennberg, P. O. *Atmos. Environ.* **2001**, *35*, 469.
(46) Finlayson-Pitts, B. J.; Pitts, J. N. *Chemistry of the Upper and Lower Atmosphere: Theory, Experiments, and Applications*; Academic Press: San Diego, CA, 1999.
(47) Arnold, S. R.; Chipperfield, M. P.; Blitz, M. A.; Heard, D. E.; Pilling, M. J. *Geophys. Res. Lett.* **2004**, *31*, L07110/1.
(48) Blitz, M. A.; Heard, D. E.; Pilling, M. J.; Arnold, S. R.; Chipperfield, M. P. *Geophys. Res. Lett.* **2004**, *31*, L06111/1.
(49) Evans, M. J.; Shallcross, D. E.; Law, K. S.; Wild, J. O. F.; Simmonds, P. G.; Spain, T. G.; Berrisford, P.; Methven, J.; Lewis, A. C.; McQuaid, J. B.; Pilling, M. J.; Bandy, B. J.; Penkett, S. A.; Pyle, J. A. *Atmos. Environ.* **2000**, *34*, 3843.